Title

Effect of interlayers and scanning strategies on through-thickness residual stress distributions in additive manufactured ferritic-austenitic steel structure

Authors

Woo, Wanchuck
Kim, Dong-Kyu
Kingston, Ed J
et al.

Publication Date

2019

DOI

10.1016/j.msea.2018.12.078

Effect of interlayers and scanning strategies on through-thickness residual stress distributions in additive manufactured ferritic-austenitic steel structure

Wanchuck Woo [a*], Dong-Kyu Kim [b*], Ed. J. Kingston [c], Vladmir Luzin [d], Floriana Salvemini [d], Michael R. Hill [e]

[a] *Neutron Science Center, Korea Atomic Energy Research Institute, Daejeon, 34057, Korea*

[b] *School of Mechanical Engineering, University of Ulsan, Ulsan, 44610, Korea*

[b] *Veqter Ltd, University Gate East, Bristol, BS1 5UB, UK*

[c] *Austrailian Nuclear Science and Technology Organization, Lucas Heights, NSW 2234, Australia*

[d] *Department of Mechanical and Aerospace Engineering, University of California, Davis, CA 95616, USA*

*Corresponding author:

Wanchuck Woo

Neutron Science Center, Korea Atomic Energy Research Institute,

Daejeon, 34057, South Korea

Phone: 82-42-868-4646, Fax: 82-42-868-4629

*Co-corresponding author:

Dong-Kyu Kim

School of Mechanical Engineering, University of Ulsan,

Ulsan, 44610, South Korea

Phone : 82-52-259-2137, Fax : 82-52-259-1680

(Manuscript to be submitted to: *Materials Science and Engineering A*)

*Author to whom correspondence should be addressed; electronic mail: chuckwoo@kaeri.re.kr

Abstract

A total of five different types of specimens were additively manufactured by directed energy deposition (DED) process. The specimens have a functionally graded material (FGM) structure, which has been deposited with variation of chemical composition of ferritic and austenitic steel powders in each interlayer on a steel substrate. Residual stress distributions were experimentally measured through the thickness of the specimens by the contour method, neutron diffraction, and deep/incremental center hole drilling. Neutron diffraction provided three orthogonal stress components in each FGM part and the results were compared to the two-dimensional stress map obtained by the contour method and confirmed its criticalities from the highly spatial resolved depth profile by the hole drilling method. Significant variations from tension to compression (up to 950 MPa) in the sine-wave stress profile were alleviated to about 430 MPa when the FGM were deposited with orthogonal or island DED scanning strategies with interlayers. Gradual changes (16.3 to 12.1 x 10^{-6} /°C) of the thermal expansion coefficient were measured among the inserted DED FGM parts and grain structure with defects along the interface was three dimensionally examined by neutron tomography.

Keywords: Directed energy deposition, Functionally graded material, Residual stress, Neutron diffraction, Deep hole drilling, Neutron tomography

1. Introduction

Additive manufacturing (AM) is defined as a process to make objects from 3D model data based on an incremental voxel-by-voxel or layer-by-layer manufacturing, as opposed to conventional subtractive engineering methodologies [1]. Thanks to the unique advantages including inherent design freedom, qualified net-shaping, and short lead times, AM has attracted much attention over past ten years and numerous vitiations of AM technologies can be broadly classified into two classes: powder bed fusion (PBF) and direct energy deposition (DED) [2,3]. The PBF utilizes laser (selective laser melting, SLM) or electron beam (electron beam melting, EBM) as heat sources to melt metal particles selectively and build up layer by layer in the powder bed, whereas the DED generates a melt pool directly from powder or wire feedstock to deposit on the object layers by using laser or electron beam energies. Extensive studies have been reported to examine the microstructure/texture [2-5], grain/interface morphologies [3-7], and tensile/fatigue properties [8,9] in AM components.

Inherently AM induces highly localized heat input on its melting pool followed by rapid solidification [3]. Instant shrinkage restricted by the surrounding cold prior materials causes detrimental tensile residual stresses and potentially degrades the fatigue strength and life of the AM products [9]. Significant efforts have been performed to understand the influence of the processing methods (PBF vs. DED) and/or deposition scanning strategies such as unidirectional, bidirectional, and island scans on residual stress distributions in various AM components by using neutron diffraction [10-18], x-ray diffraction, [19,20], contour/hole drilling method [21-23], and computational simulation [24-26]. A few parametric studies have been focused on appropriate processing and scanning strategies to mitigate or control residual stresses and distortions [10-13]. The results show that residual stresses can be reduced as decreases the scan deposition length, e.g., island size or hatch length and/or as increases the scanning speed due to the less spatial heat amounts into the AM metal

components. Sochalski-kolbus *et al*. [14] and Szost *et al*. [15] showed that the residual stresses in AM parts processed by DED are much larger than those of EBM and SLM mainly due to the absence of the powder pre-hearting stage and higher heat inputs (laser power/speed) of the DED process. A number of experimental and simulation results showed that the high tensile residual stress (close to the yield strength) is developed near the upper layers of the AM components because of the repeated thermal expansion and contraction followed by strain compatibility during consolidation [16,17,24-26].

Recently the AM technologies were further applied for manufacturing the functionally graded material (FGM), which is a class of material system with properties varying with locations by changing the chemistry or microstructure [27-30]. Carroll *et al*., [27] reported an FGM structure built from 304L stainless steel incrementally graded to Inconel 625 with 24 interlayers by reducing 4% volume of the stainless steel powder sequentially in each layer using DED process. They observed gradual hardness changes and appearance of cracks with Nb/Mo carbides as secondary phases vary along the interface. Bobbio *et al*., [28] found morphological defects and cracking due to Fe-Ni-Ti based intermetallic phases in a Ti-6Al-4V to Invar 36 (36 wt% Ni) FGM structure. FGM conceptual design further expanded to heterogeneities of microstructure and texture in a single-composed structure manufactured by different SLM processing parameters and investigated a sharp transition in mechanical properties of Inconel 718 FGM [29]. Mukherjee *et al.*, [30] reported a thermo-mechanical modeling results that the residual stresses and distortions can be minimized in a compositionally graded structure compared to the discontinuous dissimilar joint between 2.25Cr-1Mo steel/Ti-6Al-4V and an iron-nickel alloy (800H) fabricated by DED [30]. Up to date, no reports were found to examine the residual stresses in FGM structures manufactured by AM.

This paper constitutes a detailed study undertaken to obtain through-thickness distributions of residual stresses in ferritic to austenitic steel FGM specimens manufactured by DED process. Four methods of residual stress measurements were complemented in this work: neutron diffraction (ND), contour method (CM), deep hole drilling (DHD), and Incremental center-hole drilling (ICHD) [31-36]. ND has become a well-established non-destructive method for measuring residual stresses based on volume-averaged bulk measurements [31,32]. It can provide three orthogonal stress components through the thickness of the specimen within each FGM layers. The CM, a residual stress analysis method is based on measuring the surface displacements after making a cut across the sample and stress back recalculations under the assumption that the surface is returned to its original position [33,34]. It elucidates the two-dimensional stress distributions over the cross-section and the obtained widespread results are comparable to ND. The DHD, a mechanical strain relief technique allowing to measure stress along a line through the component thickness [35]. It was used to confirm the ND and CM depth profiling results with high spatial resolution and to provide the accurate position of the maximum stress and its magnitude. Finally, the ICHD utilizes the strain gauge rosette to measure the relieved strains and determines stresses near surface of about a few tens of micrometers [36].

In this paper, we present: (i) experimental results on spatial distributions of macroscopic residual stresses through the thickness of a FGM structure manufactured by DED process by using four different methods (ND, CM, DHD, and ICHD); (ii) comparison of the through-thickness stress distributions among the five different kinds of FGM specimens additively manufactured by using bidirectional, orthogonal, and island scanning strategies with the different number of interlayers; and (iii) variations of the properties such as thermal expansion coefficient, hardness and grain microstructure in the FGM parts as well as (iv) the distribution of the bulk defects inside the FGM parts using neutron tomography.

2. Additive manufacturing, Microstructure, and Thermo-mechanical Properties

As-received commercial austenitic stainless steel powder (316L, 17Cr, 12Ni, 2.5Mo, 0.03C, 0.75Si, 2.0Mn, 0.05P and balance Fe, in wt.%) and ferritic carbon steel powder (P21, 0.2C, 0.3Si, 0.3Mn, 0.03P and balance Fe in wt.%) were prepared with the particle size of 45-150 μm as summarized in Table 1. Rectangular shape (60-mm long by 20-mm wide by 15-mm thick) of specimens were additively manufactured by using DED process on a ferritic steel substrate (S45C) with the dimension of 60-mm long by 50-mm wide by 5-mm thick plate type, Fig. 1. Denoted the longitudinal (x), transverse (y), and normal (building, z) directions. The centerline is marked along the mid-length and width through the thickness of the specimen in Fig. 1a. The DED process was performed using the laser power of 200-1000 W, a scanning speed of 14.1 mm/s, a layer thickness of 250 μm, and a hatch spacing (laser beam spot size) of 400 μm under argon gas atmosphere with a pressure of 10 mbar and an oxygen of 0.2%. In order to maintain the layer thickness and hatch width of the deposition, the laser power was changed instantly by means of automatic feedback controlling system in a DED system (INSSTEK MX-400).

A total of five cases in DED FGM were fabricated by; (*Case 1*) bidirectional scan, which is a zigzag way starting from the same location among layers and creates two parts (each part with 100 wt.% ferritic and austenitic steel compositions), Fig. 1a, (*Case 2*) bidirectional scan for three parts (two parts are same with *Case 1* and one intermediate part of 50% ferritic and 50% austenitic steel composition), Fig. 1b, (*Case 3*) bidirectional scan for five parts (two parts are same with *Case 1* and three intermediate parts processed by reducing 25% volume of the stainless steel powder sequentially from the top), Fig. 1c, (*Case 4*) orthogonal scan for five parts (compositions of each part are same with *Case 3*), which is firstly scanned with vector along x and secondly along y starting from the same location among layers, Fig. 1d, and (*Case 5*) island scans in five parts (compositions of each part are same with *Case 3*), Fig.

1e. The island size of 5 x 5 mm^2 was deposited by the orthogonal manner without shifts or rotations between layers to eliminate any possible geometric complexity on residual stresses. Three samples were fabricated in each case using identical processing conditions and provided for residual stress measurements using ND, CM, and DHD (ICHD), respectively, Fig. 2.

Microstructural characterization was performed on cross-sections of each specimen. The specimens for optical microscopy (OM) were prepared by cutting with electrical discharging machining (EDM) and electrolytically etching them with the etchant of 10% perchloric acid and 90% acetic acid. A field-emission scanning electron microscope (JSM-7100F) equipped with electron backscatter diffraction (EBSD) system was utilized to analyze grain structure on the cross-section (y-z plane) with the step sizes of 0.5 μm in representative interface regions.

Fig. 3 shows a composite picture of the cross-sectional micrographs in each case. Firstly, it shows clear interfaces between parts and the shape of the melt pools resembles a localized puddle (equiaxed grain structure), which is explained by re-melting of a previously deposited layer by the consecutive one causing epitaxial grain growth along the building (z) direction [4,29]. The average grain size of the stainless steel part (~300 μm) is relatively larger than that of the ferritic steel part (~190 μm) macroscopically by OM as marked in Fig. 3a. Comparatively short (along x) and deep (along z) melting pool with equiaxed grains is known to be typical in DED [1.6]. It is because of the relatively higher heat input (generally laser power of kW) in DED contrast to lower heat input (~a few hundreds W) resulting in the typical columnar grain growth structures in PBF [12]. Besides, the ferritic steel contained parts, Fig. 3a-c, preferentially exhibit inclined equiaxed grains, which are rotated along the x axis due to the temperature gradients affecting the curvature of the solidification interface [3].

Secondly, Fig. 4 (middle) shows EBSD results of the interface taken from the marked macroscopic cross-sections (Fig. 4, top). It clearly shows the severe changes of the grain size between the ferritic and austenitic steel parts across the interface. For example, in the EBSD of *Case 1*, Fig. 4a, the average grain size near the interface was about 50 μm for the austenitic steel part and ~18 μm for the ferritic steel part as obtained by the linear intercept method. Since the cooling rate is one of the critical factors to determine the grain size, three times lower thermal conductivity of the austenitic steel (16 W/mK) than ferritic steel (43 W/mK) can lead to slower cooling and longer growth time resulting in the larger grain size of the austenitic steel part. The difference of grain size is similar when the scanning strategies is orthogonal (*Case 4*) or island (*Case 5*), as shown in Fig. 4d-e.

Noticeable macroscopic pores and defects marked in Fig. 3e and Fig. 4e (top) were further examined three dimensionally by using the DINGO neutron imaging instrument at ANSTO [37]. High spatial resolution configuration (ratio of collimator-detector length to collimator aperture equals to 1000), corresponding to a pixel size of 27 μm, was used to detect the structural defect features inside the DED FGM specimens. Projections were obtained by rotating the sample around its vertical axis (z) for 1200 angles with an equiangular spaced step of 0.3° from 0° to 360°. At each step the specimen was exposed to the neutron beam for a period of 50 seconds. The portion of the beam transmitted through the sample is converted into visible light by a 50 μm thick ^{6}LiF/ZnS scintillator and guided via a mirror to an Andor DW434 CCD camera with 2048×2028 pixels. The data sets were reconstructed with the Octopus package and visualized by AVISO 9.1 [38].

Vickers microhardness was examined across the cross-section with the step size of 0.3 mm and indentation load of 1.96 N for 10 seconds. Figure 4 (bottom) clearly shows that the micro hardness is different among parts and the distribution is inhomogeneous within the individual layer. The hardness values ranged about 200 Hv in ferritic and austenitic steel parts increase

up to 440 Hv in the interlayers. The reason is likely due to the finer grain size of the equiaxed grain structures in the gradient regions of the DED FGM structures that also can be directly shown by the EBSD results, Fig. 4 (middle) [27,29]. Two miniaturized tensile specimens (the total length of 18 mm) were prepared from each ferritic and austenitic steel parts and uniaxial tensile testing was performed at room temperature under the initial strain rate of 10^{-3} s^{-1}. The dimension of the parallel gauge was 10 mm long, 2 mm wide, and 1 mm thick. The yield strength and elongation were obtained as 1050 MPa, 0.18 for the ferritic steel and 510 MPa, 0.33 for the austenitic steel DED FGM parts, respectively.

Phase analysis was performed using x-ray diffraction. Fig. 5 shows the diffraction peaks measured at five inter-parts in *Case 3*. Other cases are similar in each part (not shown). It shows that the fcc phase in the part 1 (top layer) changes gradually to the bcc phase in the part 5, which is close to the bcc phase of the substrate. The whole peak fitting by Rietveld refinement method provides the volume fraction of the bcc phase as 0, 0.194, 0.483, 0.788, and 1.0 from part 1 to 5, respectively.

Thermal dilation experiments were performed to measure the coefficient of thermal expansion (CTE, $x10^{-6}$ /°C). The CTE sample was 30 mm long bar type with the diameter of 3 mm, which was cut by EDM from the five parts of the DED FGM in *Case 3*. Thermal expansion and contraction were recorded during heating to 1000 °C at a rate of 1 °C/s, holding for 5 min, and cooling down to room temperature at a rate of 1 °C/s.

3. Residual stress measurements

3.1. Neutron diffraction

Spatially-resolved neutron strain mapping was performed by using the KOWARI engineering strain diffractometer at ANSTO [39]. The wavelengths of 1.52 Å and 1.67 Å were selected for the diffraction planes of (311) in fcc austenitic stainless steel and (211) in

bcc ferritic steel phases at scattering angles of 89.0^o and 91.2^o, respectively. Si (400) monochromator at take-off angles of 75.9^o and 68.0° was used to produce neutrons with these wavelengths. The scattering gauge volume of the neutron beam was defined by 2 mm wide and 15 mm high input slits and a 2 mm output slit. Thus, the nominal scattering volumes of 15(x) × 2(y) × 2(z) mm^3 (mode I) was used for collecting the diffraction patterns and strain profiles through thickness of the samples. Three normal directions, x, y and z, were measured using the gauge volume. In general, the elongated gauge volume (15 mm along in the x direction) has been accepted not to cause any potential bias due to the trivial strain gradient along the x direction [32,34].

Additional longitudinal and normal strain component measurements were carried out with 2 mm size cube gauge volume using the Residual Stress Instrument (RSI) at High-flux Advanced Neutron Application Reactor, KAERI [34]. Thus, higher spatial resolution were utilized with the gauge volume of 2(x) × 2(y) × 2(z) mm^3 (mode II). The Si (220) monochromators at take-off angles 45^o produced neutrons with the wavelength of 1.46 Å for the diffraction planes (311) in fcc and (211) in bcc at scattering angles of 84.4^o and 76.2^o, respectively. A total of 12 points were measured through the thickness of the DED FGM specimens starting from 2 to 18.5 mm from the top surface with 1.5 mm steps along the centerline as shown in Fig. 2. Mostly, the measurement period was about 20 minutes for each strain component achieving a strain uncertainty of about ±100 με. Comb-like "stress free" reference samples were extracted along the centerline of the specimens by EDM and cut along the z direction. Thus, the comb consists of 5 mm long (x), 10 mm wide (y), and 5 mm deep (z) coupons. The stress-free lattice spacing (d_o) was carefully measured at the same locations of the bulk specimen with the scattering volume of 2(x) × 2(y) × 2(z) mm^3.

Diffraction peak positions were analyzed using a least squares Gaussian fitting method using instrumental data analysis programs. Once the peak position was determined, the elastic

lattice strains (ε) were calculated using $\varepsilon=-cot\theta(\theta-\theta_o)=(d-d_o)/d_o$, where the θ_o (d_o) and θ (d) are the diffraction angles (d-spacings) for the stress-free and stressed materials at each position, respectively [32]. The generalized Hooke's law was used to convert elastic strains (ε_x, ε_y, ε_z) to the residual stresses (σ_x, σ_y, σ_z) along the three orthogonal directions (x, y, and z) in a given plate. The (*hkl*)-dependent diffraction elastic constants (E) and Poisson's ratio (ν) were 183.5 GPa, 0.31 for E_{311} (fcc) and 225.5 GPa, 0.28 for E_{211} (bcc) [32]. The macroscopic residual stress (σ) at location (r) was derived from averaging phase-specific stress values according to the volume fraction (V_f) of the phases [32,40];

$$\sigma_i(r) = V_f^{bcc} \cdot \sigma_i^{bcc}(r) + (1 - V_f^{fcc}) \cdot \sigma_i^{fcc}(r) \quad ; (i = x,\ y,\ or\ z) \tag{1}$$

Note that the V_f^{bcc} is the bcc volume fraction from the part obtained by the x-ray diffraction as shown in Fig. 5.

3.2. Contour method and deep hole drilling

The contour method (CM) is a technique for the determination of the residual stress over a cross-section [33]. The displacements of the cut surface (the surface contour) are created as residual stresses are relaxed. The residual stresses are computed by applying the measured displacements inversely to an assumed flat surface contour using an elastic finite element model. One stress component normal to the cut surface can be reconstructed from a cut. The main experimental procedures include: (1) specimen cutting, (2) highly accurate surface displacement measurements, and (3) data reduction and analysis. More detailed description could be found in ref. 33.

Each DED FGM specimen was cut in half at the mid-length position as shown Fig. 2. This was done by using EDM with a 100 μm diameter brass wire. To minimize cutting induced stresses, the specimen was submerged into the temperature-controlled de-ionized

water and performed the ‘‘skim cut’’ with the cutting speed of 0.15 mm/min. After cutting, the normal direction (x) displacements on the cut surfaces were measured using a scanning confocal laser probe with an accuracy of ±0.02 μm. The maximum peak-to-valley range of the contour was about ±30 μm and fitted to a smooth analytical surface for stress calculation. A three-dimensional elastic finite element model in ABAQUS/Standard 6.12 meshed geometries as hexahedral elements (C3D20R) and calculates linear elastic stress to provide the stress field normal to the plane of sectioning (σ_x) in the specimen. The elastic moduli (E) and Poisson’s ratio (v) were 193 GPa, 0.3 for fcc, 207 GPa, 0.3 for bcc, and 200 GPa, 0.3 for the substrate, respectively. Note that the elastic constants for each part of the DED FGM specimen were derived by the rule-of-mixture principle accordingly to the measured phase volume fraction.

Since the DED FGM component can contains high magnitude, tri-axial residual stresses, the incremental deep hole drilling (iDHD) method was applied. Details are well described in ref. 33. In brief, the iDHD technique is an advanced DHD method by considering plastic relaxation during the trepanning process. The main difference of the iDHD is that the core (diameter of 5 mm) is extracted in incremental machining steps and the diameter of the reference hole (diameter of 1.5 mm) is measured between each increment. The iDHD technique was used for a longitudinal (σ_x) and transverse stress (σ_y) measurements with 2 mm depth step (total of 12 points) though the thickness of the DED FGM specimens in *Cases 1*, *3*, and *5*. Besides, a DHD experiment was performed through the side surface at 5 mm from the top surface at *Case 4* in Fig. 2 in order to confirm the a longitudinal (σ_x) and normal stress (σ_z) components between DHD and ND. The elastic moduli (E) and Poisson’s ratio (v) are same with the contour method.

Incremental center-hole drilling (ICHD) method is a semi-invasive, mechanical strain relief technique to determine stresses near surface [36]. The ICHD procedure involves

surface preparation, gauge bonding, and circuit connections. The surface firstly degreases and neutralized to remove any oxides and oils. The strain gauge rosettes of type EA-06-031RE-120 adhered with gauge elements aligned to the x and y directions. Then a quarter Wheatstone bridge circuit was formed by soldering the lead wires to the terminals of the gauge. Finally three axis drilling machine makes a small hole into the surface at the center of a strain gauge rosette and measuring the relieved strains. ICHD was performed for three specimens (*Cases 1, 3,* and *5*) from the top surface up to 500 μm with incremental depth drilling in steps of 25 μm. The strains were measured by the elements of the strain gauge rosette and the residual stresses were calculated based on ASTM-E837-13a [36]. The ICHD test was performed prior to the iDHD measurements.

4. Results

4.1. Residual stresses by neutron diffraction

Fig. 6 shows the distributions of residual stresses through the thickness of the five cases of the FGM specimens manufactured by DED process. The nominal compositional ratio between the ferritic and austenitic steels was marked in each part from the top surface. The stress uncertainties were mostly less than ± 60 MPa. Firstly for the *Case 1* in Fig. 6a, the through-thickness stress profiles of the σ_x show that tensile stresses (~300 MPa) near the top surface through austenitic steel part continuously turns into compression (up to -470 MPa) at the ferritic steel part in the middle and returns to tension at the substrate bottom of the specimen. Such stress balanced "C" shape was also investigated in the stress depth profile of σ_y, though with smaller magnitude than σ_x. Owing to the accumulated thermal expansion/contraction and non-uniform plastic flow, higher residual stresses are often found near to the top surface of multipass thick welds [34,41].

Meanwhile, *Case 2*, Fig. 6b, shows that the stress profiles significantly fluctuate demonstrating a sine-wave-like distribution through the thickness of the specimen. Such fluctuation has been suggested as a typical stress profile feature through the thickness of thick weldments in the consideration of a stress balancing mechanism of stress redistribution [42]. In particular, the σ_x and σ_y show significant changes from tension to compression (470 to -360 MPa) in the mixture part between ferritic and austenitic steels (marked by an arrow). Note that the σ_x of 470 MPa at 2 mm below the top surface corresponds to the 92% of the yield strength (510 MPa) of the DED stainless steel part. Mukherjee *et al.* [30] reported a computational result showing sharp changes of the σ_x in the interlayer of a 2.25Cr-1Mo steel/Ti-6Al-4V and an iron-nickel alloy DED dissimilar/FGM structure. Current experimental result shows that similar variations exist in the DED FGM structure. It becomes more severe in the five layered DED FGM specimen *Case 3*. Fig. 6c shows that the abrupt change from tension to compression ($\Delta\sigma = \sigma_{max} - \sigma_{min}$ = 950 MPa) occurs when across the 2nd interface from 5 to 8 mm from the top surface. When the FGM are interlayered by using orthogonal (*Case 4*) and island (*Case 5*) DED scanning strategies, the maximum-to-minimum range ($\Delta\sigma$) becomes less extremely reduced from 950 MPa to 680 MPa and 430 MPa for *Case 4* and *Case 5* as shown in Fig. 6d-e, respectively. This effect can be associated with less heat input and effective heat-flow dissipation achieved by the alternating scans and discussed in details in section 5.1.

The stress distribution of the normal component (σ_z) is clearly different between *Cases 1* and *2*, Fig. 6a-b. In contrast to the minor fluctuation of σ_z within ±50 MPa in *Case 1*, as marked by a dotted arrow in Fig. 6b, *Case 2* shows noticeable increase in tensile stress up to 350 MPa at the depth of 6.5 mm. In order to resolve the sampling volume issue (described in section 4.1), Fig. 6a-b compares the σ_z profiles obtained from cube gauge volume of 8 mm^3 (2x2x2, mode II) and elongated gauge volume of 60 mm^3 (2x2x15, mode I) and confirmed

similar results. This large σ_z is also observed over 260 MPa among other *Cases 3*, *4*, and *5* as shown in Fig. 6c-e. Besides, the neutron diffraction results (σ_x and σ_z) at 5 mm depth in *Case 4* were confirmed by the DHD analysis as marked in Fig. 6d. Thus, it is suggested that there are significant amounts of stresses along the building direction (σ_z) in the DED FGM structure. It has been mainly attributed to the thermal excursion and accumulation along the building direction during additive manufacturing and the plane stress condition ($\sigma_z = 0$) or hydrostatic stress condition ($\sigma_x \approx \sigma_y \approx \sigma_z$) is not valid in the middle of the DED and/or FGM DED structures [10,21]. Besides, it assumes a presence of significant shear stress components, therefore, manifesting rotation of the principal axes of the stress tensor as a function of depth [26].

4.2. Residual stresses by contour and deep hole drilling methods

Fig. 7 shows the results from the contour method (CM) as two-dimensional maps of the σ_x. The stress uncertainty for the CM measurements was about ± 30 MPa. Through-thickness profiles were extracted from the maps along the centerlines and compared to the ND results. Firstly, the residual stress maps show clear differences among the cases. When observed the stress profiles of the *Cases 1*, *2*, and *3*, which were all processed by the same bidirectional scan as shown in Fig. 1a-c, tensile stresses near the top surface continuously change to the compression in the middle parts of the DED FGM specimens to balance the stress state (Fig. 7a-c). Considering three five-layered systems, the through-thickness stress distribution becomes relatively homogeneous in *Cases 4* and *5* when compared to *Case 3*. The extracted by CM stress profiles show that the difference of stress values ($\Delta\sigma$) in *Cases 1*, *2*, and *3* clearly decreases when the DED scanning strategies are adopted by the orthogonal (*Case 4*) or island (*Case 5*) scans as shown in Fig. 7d-e, respectively. For example, the maximum-to-

minimum difference of the stress ($\Delta\sigma_x$) decreases from 770 MPa in *Case 3* (bidirectional scan) to 450 MPa in *Case 4* as marked in Fig. 7c-d

Finally, Fig. 8 shows the residual stress profiles obtained from the DHD measurements along the centerline (Fig. 2) through sample thickness in *Cases 1*, *3*, and *5*. It shows fine (0.2 mm) through-depth resolution. Owing to no severe plastic relaxation of the stressed region in the whole thickness of the specimen, the iDHD results were similar to DHD results. Fig. 8 shows that the range of stress values ($\Delta\sigma$) is relatively decreased in *Case 5* when compared to *Cases 1* and *3* in both σ_x and σ_y DHD profiles. Besides, the DHD results elucidate the maximum stress location near top surface and the minimum at 8 mm depth in the mixture parts of *Cases 3* and *5* in Fig. 8b-c. Here we include neutron diffraction (ND) results and confirmed overall trends are similar between DHD and ND. There is a slight difference of less than ±100 MPa in the middle parts of the DED FGM *Case 5*, Fig. 8c. The difference was confirmed by the ND experiments measured by using higher spatial resolution (mode II) as marked ND (II). Several uncertainties have been suggested for the discrepancy including misalignment of the reference hole, calibration and curve-fitting of the air sensing probe, and material constant/microstructure effects [35,36].

5. Discussion

5.1. Through-thickness distribution of residual stresses in additive manufactured FGM

The discussion starts by examining the significant changes of the residual stress profiles in the DED FGM structure. Among *Cases 1*, *2*, and *3*, the interlayer causes sine-wave like fluctuations from tension near the top surface to compression in the 2nd or 3rd layers ($\Delta\sigma$ = 950 MPa) through the thickness of the specimens, Fig. 6a-c. Significant tensile stresses are often found along the interface between the ferritic and austenitic steel welds due to the large mismatch of the coefficient of thermal expansion (CTE, x10^{-6} /°C) of the two dissimilar

materials [43]. Fig. 9 shows the CTE variations in each part of the current DED FGM specimen measured 16.3 for the stainless steel part and 12.0 for the ferritic steel part by analyzing the linear expansion from room temperature to 100 °C. It provides the CTE difference (ΔCTE) of 4.3 in the entire DED FGM structure. Although the CTE decreases with a reduction in the stainless steel composition, most of the ΔCTE (~3.1) occurs when the steel added by ~50%. Thus, it can be the reason of the significant stress difference was observed in the 2nd (*Case 2*) and 3rd (*Case 3*) parts as shown in Fig. 6b-c. Indeed, the two dimensional stress map by CM clearly shows the inhomogeneity through the thickness among the parts in *Cases 2* and *3* in Fig. 7b-c. The current ΔCTE of 3.1 can cause a mismatch in terms of thermal strain (ε^{th}) of about 4,600 με based on a simple estimation (ε^{th} = ΔCTE x ΔT), supposed that the peak temperature of the laser beam is 1500 °C and cools down to room temperature during DED process [24,30]. It is corresponding to about 930 MPa with the elastic constant of 203 GPa in the interlayer of *Case 3* and the value is comparable to the range of stress ($\Delta\sigma$ = ~950 MPa) in Fig. 6c.

Secondly, let us discuss about the influence of the scanning strategy on the residual stress distributions in the DED FGM structure. The range of stress values ($\Delta\sigma$) significantly decreases from 950 MPa (*Case 3*) to ~ 430 MPa (*Cases 4* and *5*) in Fig. 6c-e. It is consistent among ND, CM, and DHD as shown in Fig. 6-8. The reason is attributed to the origin of residual stresses in additive manufacturing processes, for example, the spatial temperature gradient (localized heating/cooling by the heat source), followed by thermal expansion/contraction and strain compatibility due to uneven distribution of plastic flow [3,13,23]. Thus, shorter deposition length (scanning in smaller islands) and/or less heat accumulation (orthogonal scan) strategies can mitigate residual stresses because of the less amount of heat input and moderate thermal gradients, and effective heat source dispersion along multiple directions rather than heat accumulation along the building direction,

respectively [44,45]. As a result, the island scan (*Case 5*) shows much smaller grain size compared to the bidirectional scan (*Case 3*) in Fig. 4. The bidirectional scan (*Case 3*) exhibits an oriented solidification grain structure between layers as marked by arrows in Fig. 3d, whereas the orthogonal scan (*Case 4*) has various maximum heat flow vectors oriented to different directions among layers as marked in Fig. 3d.

5.2. Residual stress distribution near surface and defects inside FGM

Since the fracture mechanics focuses on stress concentrations around localized defects and the stress-driven crack initiation and propagation, the residual stress distribution near surface has an importance for the DED FGM specimens [9,26,29]. Fig. 10 shows that the compressive stress (σ_x) of -200 MPa at 25 μm depth changes to tension reaching 300 MPa at ~200 μm and gradually decrease to -200MPa at 500 μm in *Case 1*. It is a comparable to σ_y and other cases. A number of studies reported residual stresses near-to-surface distributions in various AM components [20,24,25,30,46]. For example, tensile stresses of 150 and 200 MPa were analyzed by x-ray diffraction in island and unidirectional scanned SLM stainless steel specimens, respectively [20,25] and over 435 MPa in unidirectional scanned SLM steel by hole drilling [46]. Meanwhile, similar to the current study, noticeable compression stresses (ranging from -50 to -250 MPa) were simulated in a unidirectional DED stainless steel [30]. Since the SLM is typically processed with lower energy density (<100 J/mm^3 for Ti-6Al-4V) on a thin layer than DED (90-220 J/mm^3), it is suggested that the SLM leads to the fast cooling rates, higher thermal gradients, and material hardening resulting in higher tensile stresses compared to the DED in general [1].

The occurrence of macroscopic defects in the DED FGM specimen was assessed by neutron diffraction tomography with actual spatial resolution of about 50 μm. The transversal (across x) and longitudinal (along x) cross-section of the neutron tomographic reconstructions

were used for inspection of internal defects, Fig. 11. No clear defects are detectable in *Case 1* (Fig. 11a) and *Cases 2*, *3*, and *4* (not shown), while a number of defects were found in *Case 5* (Fig. 11b). Neutron tomography shows that the three dimensional distribution of defects is preferentially located along the corners of the DED islands and have an equivalent diameter (the diameter of the spherical particle of same volume) in the range of 100 - 900 μm, Fig. 11c. Porosities and lack-of-fusion voids are typical defects in AM and often reported in the case of an island scanning build components [5]. Three main mechanisms are summarized for the defects: (i) entrapped vapor in the keyhole mode due to very high power intensity; (ii) captured gas during powder atomization; and (iii) lack of fusion by inadequate penetration [47]. It is suggested that the observed defects are the lack-of-fusion driven pores, Fig. 11c, which are normally formed along the corners of the previously deposited layers (marked region of interest in Fig. 11b) as highlighted in Fig. 11d.

6. Conclusions

1. This paper constitutes detailed results obtained from five kinds of directed energy deposition (DED) functionally graded material (FGM) specimens. Using variable compositional ratio between ferritic and austenitic steel, two (*Case 1*), three (*Case 2*), and five (*Case 3*) layered FGM structures were additively manufactured with bidirectional scanning on a steel substrate using DED process. Two more specimens were prepared by the orthogonal (*Case 4*) and island (*Case 5*) scanning strategies in each layer for comparison. Microstructure, thermal, mechanical properties, and residual stresses were examined through the thickness of the DED FGM specimens.

2. Distinct microstructural features were investigated in the ferritic and austenitic steel DED FGM parts. Both parts show an equiaxed grain structure created by the epitaxial grain growth

along the building direction (z). The ferritic steel part shows preferentially inclined grain structure in the bidirectional scan (*Cases 1*, *2*, and *3*), whiles it becomes less preferred in the orthogonal (*Case 4*) and island scan (*Case 5*) due to the mixture of the scanning strategies between interlayers. The austenitic steel part shows much larger grain size (~300 μm) compared to the ferritic steel part (~190 μm). Furthermore, the interface characterization by EBSD confirms significant decreases of the grain size when across from the austenitic to the ferritic steel parts. Besides, island scanning build-up (*Case 5*) leads to further smaller grain size (~60 μm) than the bidirectional scan (~110 μm) near the interface of the DED FGM components.

3. The yield strength and elongation were determined as 510 MPa, 0.33 for the austenitic steel part and 1050 MPa, 0.18 for the ferritic steel part of the FGM DED specimen, respectively. The hardness of about 200 Hv in the steel (or stainless steel) part increases up to 440 Hv in the mixed parts as the grain size decreases. The coefficient of thermal expansion (CTE, $x10^{-6}$/°C) decreases from 16.3 to 12.0 as the composition changes from the austenitic to ferritic steel parts. Most of the CTE difference (ΔCTE) of ~3.1 occurs when the ferritic steel phase added by ~50% in the DED FGM part.

4. Neutron diffraction (ND), contour method (CM), deep hole drilling (DHD), and incremental center-hole drilling (ICHD) were applied to obtain full-field knowledge of the magnitudes and spatial distributions of the residual stresses through the thickness of the DED FGM structures.

- From the top of the specimen, near-surface stresses were investigated by ICHD technique and compressive stresses (σ_x and σ_y) of about -200 MPa were found at 25 μm depth. The compressive stress changes to tension of approximately 300 MPa magnitude

at 200 μm depth. Then, it reaches tension of 410 MPa (~80% of yield strength) at 2 mm depth and significantly changes from tension to compression (up to 950 MPa) as a sine-wave stress profile analyzed by DHD and ND in *Cases 1*, *2*, and *3*.

- The range of stress values ($\Delta\sigma$) is alleviated to 680 MPa when the FGM are interlayered with the orthogonal scan (*Case 4*) and further reduced to 430 MPa for the island scan (*Case 5*). It is consistent with the two dimensional stress mapping results of CM. It concludes that the large $\Delta\sigma$ observed in the bidirectional can be significantly reduced when orthogonal or island DED scanning strategies are adopted.
- There is a significant amount of the normal stress (σ_z) along the building direction in the DED FGM structure. Both ND and DHD measurements elucidate strong tension up to 350 MPa at 6.5 mm depth.

5. Island scanning strategy without shift and rotation between layers causes a number of internal defects in the DED FGM specimen. Neutron tomography shows that the defects have an equivalent diameters of 100 to 900 μm and located along the corner junctions of the interfacing islands. The main cause of porosities is suggested to be the lack-of-fusion defects by inadequate penetration along the edge of the previously deposited layer. Meanwhile, no clear macroscopic defects were investigated in the case of the bidirectional and orthogonal scanning cases.

Acknowledgements

This work was supported by the National Research Foundation of Korea (NRF) grant funded by the Korean government (No. NRF-2017M2A2A6A05017653) and the Australian Nuclear Science and Technology Organization (neutron proposal P5085).

References

[1] D. Herzog, V. Seyda, E. Wycisk, C. Emmelmann, Additive manufacturing of metals, Acta Mater. 117 (2016) 371-392.

[2] W.J. Sames, F.A. List, S. Pannala, R.R. Dehoff, S.S. Babu, The metallurgy and processing science of metal additive manufacturing, Inter. Mater. Reviews 61 (2016) 315-360.

[3] T. DebRoy, H.L. Wei, J.S. Zuback, T. Mukherjee, J.W. Elmer, J.O. Milewski, A.M. Beese, A. Wilson-Heid, A. De, W. Zhang, Additive manufacturing of metallic components – process, structure and properties, Prog. Mater. Sci. 92 (2018) 112-224.

[4] A. Haider, G. Hassan, M. Kamran, Effect of scanning strategies on residual stress and mechanical properties of Selective Laser Melted Ti6Al4V, Mater. Sci. Eng. A (2018) 175-187.

[5] L. Thijs, K. Kempen, J.-P. Kruth, J.V. Humbeeck, Fine-structured aluminium products with controllable texture by selective laser melting of pre-alloyed AlSi10Mg powder, Acta Mater. 61 (2013) 1809-1819.

[6] N. Raghavan, R. Dehoff, S. Pannala, S. Simunovic, M. Kirka, J. Turner, N. Carlson, S.S. Babu, Numerical modeling of heat-transfer and the influence of process parameters on tailoring the grain morphology of IN718 in electron beam additive manufacturing, Acta Mater. 112 (2016) 303-314.

[7] Z.H. Liu, D.Q. Zhang, S.L. Sing, C.K Chua, L.E. Loh, Interfacial characterization of SLM parts in multi-material processing: Metallurgical diffusion between 316L stainless steel and C18400 copper alloy, Mater. Char. 94 (2014) 116-125.

[8] K.G. Prashanth, S. Scudino, J. Eckert, Defining the tensile properties of Al-12Si parts produced by selective laser melting, Acta Mater. 126 (2017) 25-35.

[9] A. Riemer, S. Leuders, M. Thöne, H.A. Richard, T. Tröster, T. Niendorf, On the fatigue crack growth behavior in 316L stainless steel manufactured by selective laser melting, Eng. Frac. Mech. 120 (2014) 15-25.

[10] P. Rangaswamy, M.L. Griffith, M.B. Prime, T.M. Holden, R.B. Rogge, J.M. Edwards, R.J. Sebring, Residual stresses in LENS components using neutron diffraction and contour method, Mater. Sci. Eng. A 339 (2005) 72-83.

[11] M.F. Zaeh, G. Branner, Investigation on residual stress and deformation in selective laser melting, Prod. Eng. Res. Devel. 4 (2010) 35-45.

[12] A.S. Wu, D.W. Brown, M. Kumar, G.F. Gallegos, W.E. King, An experimental investigation into additive manufacturing-induced residal stresses in 316L stainless steel, Matall. Mater. Trans. A 45 (2014) 6260-6270.

[13] N. Nadammal, S. Cabeza, T. Mishurova, T. Thiede, A. Kromm, C. Seyfert, L. Farahbod, C. Haberland, J.A. Schneider, P.D. Portella, G. Bruno, Effect of hatch length on the development of microstructure, texture and residual stresses in selective laser melted superalloy Inconel 718, Mater. Deg. 134 (2017) 139-150.

[14] L.M. Sochalski-Kolbus, E.A. Payzant,P.A. Cornwell, T.R. Watkins, S.S. Babu, R.R. Dehoff, M. Lorzenz, O. Ovchinnikova, C. Duty, Comparison of residual stresses in Inconel 718 simple parts made by electron beam melting and direct laser metla sintering, Matall. Mater. Trans. A, 46 (2015) 1419-1432.

[15] B.A. Szost, S. Terzi, F. Martina, D. Boisselier, A. Prytuliak, T. Pirling, M. Hofmann, D.J. Jarvis, A comparative study of additive manufacturing techniques: Residual stress and microstructural analysis of CLAD and WAAM printed Ti-6Al-4V components, Mater. Deg. 89 (2016) 559-567.

[16] Z. Wang, E. Denlinger, P. Michaleris, A.D. Stoica, D. Ma, A.M. Beese AM, Residual stress mapping in Inconel 625 fabricated through additive manufacturing: Method for neutron

diffraction measurements to validate thermomechanical model predictions, Mater. Deg. 113 (2017) 169-177.

[17] K. An, L. Yuan, L. Dial, I Spinelli, A.D. Stoica, Y. Gao, Neutron residual stress measurement and numerical modeling in a curved thin-walled structure by laser powder bed fusion additive manufacturing, Mater. Deg. 135 (2017) 122-132.

[18] Z. Wang, A.D. Stoica, D. Ma, A.M. Beese, Stress relaxation in a nickel-base superalloy at elevated temperatures with in situ neutron diffraction characterization: Application to additive manufacturing, Mater. Sci. Eng. A, 714 (2018) 75-83.

[19] Y. Liu, Y. Yang, D. Wang, A study on the residual stress during selective laser melting (SLM) of metallic powder, Int. J. Adv. Manuf. Technol. 87 (2016) 647-656.

[20] T. Simson, A. Emmel, A. Dwars, J. Böhm, Residual stress measurements on AISI 316L samples manufactured by selective laser melting, Additive Manuf. 17 (2017) 183-189.

[21] R.J. Moat, A.J. Pinkerton, L. Li, P.J. Withers, M. Preuss, Residual stresses in laser direct metal deposited Waspaloy, Mater. Sci. Eng. A, 528 (2011) 2288-2298.

[22] B. Vrancken, V. Cain, R. Knutsen, J.V. Humbeeck, Residual stress via the contour method in compact tension specimens produced via selected laser melting, Scripta Mater. 87 (2014) 29-32.

[23] E.R. Denlinger, J.C. Heigel, P. Michaleris, T.A. Palmer, Effect of inter-layer dwell time on distorsion and residual stress in additive manufacturing of titanium and nickel alloys, J. Mater. Proces. Technol. 215 (2015) 123-131.

[24] Y.P. Yang, M. Jamshidinia, P. Boulware, S.M. Kelly, Prediction of microstructure, residual stress, and deformation in laser powder bed fusion process, Comp. Mech. 61 (2018) 61, 599-615.

[25] O. Fergani, F. Berto, T. Welo, S.Y. Liang, Alalytical modeling of resiudal stress in additive manufacturing, Fat. Frac. Eng. Mater. Struc. 40 (2017) 971-978.

[26] T. Mukherjee, W. Zhang, T. DebRoy, An improved prediction of residual stresses and distortion in additive manufacturing, Comp. Mater. Sci. 126 (2017) 360-372.

[27] B.E. Carroll, R.A. Otis, J.P. Borgonia, J. Suh, R.P. Dillon, A.A. Shapiro, D.C. Hofmann, Z.-K. Liu, A.M. Beese, Functionally graded material of 304L stainless steel and inconel 625 fabricated by directed energy deposition: Characterization and thermodynamic modeling, Acta Mater. 108 (2016) 46-54.

[28] L.D. Bobbio, R.A. Otis, J.P. Borgonia, R.P. Dillon, A.A. Shapiro, Z.-K. Liu, A.M. Beese, Additive manufacturing of a functionally graded material from Ti-6Al-4V to Invar: Experimental characterization and thermodynamic calculations, Acta Mater. 127 (2017) 133-142.

[29] V.A. Popovich, E.V. Borisov, A.A. Popovich, V.Sh. Sufiiarov, D.V. Masaylo, L. Alzina, Functionally graded Inconel 718 processed by additive manufacturing: Crystallographic texture, anisotropy of microstructure and mechanical properties, Mater. Des. 114 (2017) 441-149.

[30] T. Mukherjee, J.S. Zuback, W. Zhang, T. DebRoy, Residual stresses and distorsion in additively manufactured compositionally graded and dissimilar joints, Comp. Mater. Sci. 143 (2018) 325-337.

[31] A.J. Allen, M.T. Hutchings, C.G. Winsor, C. Andreani, Neutron diffraction methods for the study of residual stress fields, Adv. Phys. 34 (1985) 445-473.

[32] M.T. Hutchings, P.J. Withers, T.M. Holden, T. Lorentzen, Introduction to the Characterization of Residual Stress by Neutron Diffraction, first ed., Taylor and Francis, London, 2005.

[33] M.B. Prime, Cross-sectional mapping of residual stresses by measuring the surface contour after a cut, J. Eng. Mater. Tech. Trans. ASME, 123 (2001) 162-168.

[34] W. Woo, G.B. An, E.J. Kingston, A.T. DeWald, D.J. Smith, M.R. Hill, Through-thickness distributions of residual stresses in two extreme heat-input thick welds: A neutron diffraction, contour method and deep hole drilling study, Acta Mater. 61 (2013) 3564-3574.

[35] D.M. Goudar, C.E. Truman, D.J. Smith, Evaluating uncertainty in residual stress measured using the deep-hole drilling technique, Strain, 47 (2011) 62-74.

[36] D. George, E. Kingston, D.J. Smith, Measurement of through-thickness stresses using small holes, J. Strain. Anal. Eng. Des. 37 (2002) 125-139.

[37] U. Garbe, T. Randall, C. Hughes, G. Davidson, S. Pangelis, S. Kennedy, A New Neutron Radiography/Tomography/Imaging Station DINGO at OPAL, Physics Procedia. 69 (2015) 27-32.

[38] M. Dierick, B. Masschaele, L. Van Hoorebeke, Octopus, a fast and user-friendly tomographic reconstruction package developed in LabView, Meas. Sci. Tech. 15 (2004) 1366-1370.

[39] A. Brule, O. Kristein, Residual stress diffractometer KOWARI at the Australian research reactor OPAL: Status of the project, Physica B: Condensed Matter. 385-386 (2006) 1040-1042.

[40] V. Luzin, K. Thorogood, J.R. Griffiths, C.J. Davidson, T.R. Finlayson, Residual stress in metal-matrix composite cylinder measured by neutron diffraction and contour method residual stresses, in ICRS-10 Materials Research Forum, Materials Research Proc. (2016) 401-406.

[41] D.J. Smith, P.J. Bouchard, D. George, Measurement and prediction of residual stresses in thick-section steel welds, J. Strain Anal. Eng. Deg. 35 (2000) 287-305.

[42] K. Masubuchi, Analysis of welded structures, first ed., Pergamon, New York, 1980, Ch. 6. Distribution of residual stresses in weldments, pp. 225-232.

[43] W. Woo, G.B. An, C.E. Truman, W. Jiang, M.R. Hill, Two-dimensional mapping of residual stresses in a thick dissimilar weld using contour method, deep hole drilling, and neutron diffraction, J. Mater. Sci. 51 (2016) 10620-10631.

[44] M. Gao, Z. Wang Z, X. Li, X. Zeng, The effect of deposition patterns on the deformation if substrates during direct laser fabrication, J. Eng. Mater. Tech. 135 (2013) 034502.

[45] H.L. Wei, J. Mazumder, T. DebRoy, Evolution of solidification texture during additive manufacturing, Scientific Report, 5 (2015) 16446.

[46] C. Casavola, S.L. Campanelli, C. Pappalettere, Preliminary investigation on distribution of residual stress generated by the selective laser melting process, J. Strain Analysis, 44 (2009) 93-104.

[47] K. Darvish, Z.W. Chen, T. Pasang, Reducing lack of fusion during selective laser melting of CoCrMo alloy: Effect of laser power on geometrical features of tracks, Mater. Des. 112 (2016) 357-366.

Effect of interlayers and scanning strategies on through-thickness residual stress distributions in additive manufactured ferritic-austenitic steel structure

Wanchuck Woo [a*], Dong-Kyu Kim [b*], Ed. J. Kingston [c], Vladmir Luzin [d], Floriana Salvemini [d], Michael R. Hill [e]

[a] *Neutron Science Center, Korea Atomic Energy Research Institute, Daejeon, 34057, Korea*

[b] *School of Mechanical Engineering, University of Ulsan, Ulsan, 44610, Korea*

[b] *Veqter Ltd, University Gate East, Bristol, BS1 5UB, UK*

[c] *Austrailian Nuclear Science and Technology Organization, Lucas Heights, NSW 2234, Australia*

[d] *Department of Mechanical and Aerospace Engineering, University of California, Davis, CA 95616, USA*

*Corresponding author:

Wanchuck Woo

Neutron Science Center, Korea Atomic Energy Research Institute,

Daejeon, 34057, South Korea

Phone: 82-42-868-4646, Fax: 82-42-868-4629

*Co-corresponding author:

Dong-Kyu Kim

School of Mechanical Engineering, University of Ulsan,

Ulsan, 44610, South Korea

Phone : 82-52-259-2137, Fax : 82-52-259-1680

(Manuscript to be submitted to: *Materials Science and Engineering A*)

*Author to whom correspondence should be addressed; electronic mail: chuckwoo@kaeri.re.kr

Abstract

A total of five different types of specimens were additively manufactured by directed energy deposition (DED) process. The specimens have a functionally graded material (FGM) structure, which has been deposited with variation of chemical composition of ferritic and austenitic steel powders in each interlayer on a steel substrate. Residual stress distributions were experimentally measured through the thickness of the specimens by the contour method, neutron diffraction, and deep/incremental center hole drilling. Neutron diffraction provided three orthogonal stress components in each FGM part and the results were compared to the two-dimensional stress map obtained by the contour method and confirmed its criticalities from the highly spatial resolved depth profile by the hole drilling method. Significant variations from tension to compression (up to 950 MPa) in the sine-wave stress profile were alleviated to about 430 MPa when the FGM were deposited with orthogonal or island DED scanning strategies with interlayers. Gradual changes (16.3 to 12.1 x 10^{-6} /°C) of the thermal expansion coefficient were measured among the inserted DED FGM parts and grain structure with defects along the interface was three dimensionally examined by neutron tomography.

Keywords: Directed energy deposition, Functionally graded material, Residual stress, Neutron diffraction, Deep hole drilling, Neutron tomography

1. Introduction

Additive manufacturing (AM) is defined as a process to make objects from 3D model data based on an incremental voxel-by-voxel or layer-by-layer manufacturing, as opposed to conventional subtractive engineering methodologies [1]. Thanks to the unique advantages including inherent design freedom, qualified net-shaping, and short lead times, AM technology has drawn great interest over past ten years and its numerous variations can be broadly classified into two classes: powder bed fusion (PBF) and direct energy deposition (DED) [2,3]. The PBF utilizes laser (selective laser melting, SLM) or electron beam (electron beam melting, EBM) as heat sources to melt metal particles selectively and build up layer by layer in the powder bed, whereas the DED generates a melt pool directly from powder or wire feedstock to deposit on the object layers by using laser or electron beam energies. Extensive studies have been reported to examine the microstructure/texture [2-5], grain/interface morphologies [3-7], and tensile/fatigue properties [8,9] in AM components.

Inherently AM induces highly localized heat input on its melting pool followed by rapid solidification [3]. Instant shrinkage restricted by the surrounding cold prior materials causes detrimental tensile residual stresses and potentially degrades the fatigue strength and life of the AM products [9]. Significant efforts have been performed to understand the influence of the processing methods (PBF vs. DED) and/or deposition scanning strategies such as unidirectional, bidirectional, and island scans on residual stress distributions in various AM components by using neutron diffraction [10-18], x-ray diffraction, [19,20], contour/hole drilling method [21-23], and computational simulation [24-26]. A few parametric studies have been focused on appropriate processing and scanning strategies to mitigate or control residual stresses and distortions [10-13]. The results show that residual stresses can be reduced as decreases the scan deposition length, e.g., island size or hatch length and/or as increases the scanning speed due to the less spatial heat amounts into the AM metal

components. Sochalski-kolbus *et al*. [14] and Szost *et al*. [15] showed that the residual stresses in AM parts processed by DED are much larger than those of EBM and SLM mainly due to the absence of the powder pre-hearting stage and higher heat inputs (laser power/speed) of the DED process. A number of experimental and simulation results showed that the high tensile residual stress (close to the yield strength) is developed near the upper layers of the AM components because of the repeated thermal expansion and contraction followed by strain compatibility during consolidation [16,17,24-26].

Recently the AM technologies were further applied for manufacturing the functionally graded material (FGM), which is a class of material system with properties varying with locations by changing the chemistry or microstructure [27-30]. Carroll *et al*., [27] reported an FGM structure built from 304L stainless steel incrementally graded to Inconel 625 with 24 interlayers by reducing 4% volume of the stainless steel powder sequentially in each layer using DED process. They observed gradual hardness changes and appearance of cracks along the interface due to the Nb/Mo carbides as a secondary phase. Bobbio *et al*., [28] found morphological defects and cracking due to Fe-Ni-Ti based intermetallic phases in a Ti-6Al-4V to Invar 36 (36 wt% Ni) FGM structure. FGM conceptual design further expanded to heterogeneities of microstructure and texture in a single-composed structure manufactured by different SLM processing parameters and investigated a sharp transition in mechanical properties of Inconel 718 FGM [29]. Mukherjee *et al*., [30] reported a thermo-mechanical modeling result that the residual stresses and distortions can be minimized in a compositionally graded structure compared to the discontinuous dissimilar joint between 2.25Cr-1Mo steel/Ti-6Al-4V and an iron-nickel alloy (800H) fabricated by DED [30]. Although the DED FGM structure attracts high industrial attention to apply for the ferritic to austenitic steel joints of nozzle components and piping systems in nuclear power plants and

pressure vessels, no reports were found in terms of the residual stress distributions through the thickness of the components up to date.

This paper constitutes a detailed study undertaken to obtain through-thickness distributions of residual stresses in ferritic to austenitic steel FGM specimens manufactured by DED process. Four methods of residual stress measurements were complemented in this work: neutron diffraction (ND), contour method (CM), deep hole drilling (DHD), and Incremental center-hole drilling (ICHD) [31-36]. ND has become a well-established non-destructive method for measuring residual stresses based on volume-averaged bulk measurements [31,32]. It can provide three orthogonal stress components through the thickness of the specimen within each FGM layers. The CM, a residual stress analysis method is based on measuring the surface displacements after making a cut across the sample and stress back recalculations under the assumption that the surface is returned to its original position [33,34]. It elucidates the two-dimensional stress distributions over the cross-section and the obtained widespread results are comparable to ND. The DHD, a mechanical strain relief technique allowing to measure stress along a line through the component thickness [35]. It was used to confirm the ND and CM depth profiling results with high spatial resolution and to provide the accurate position of the maximum stress and its magnitude. Finally, the ICHD utilizes the strain gauge rosette to measure the relieved strains and determines stresses near surface of about a few tens of micrometers [36].

In this paper, we present: (i) experimental results on spatial distributions of macroscopic residual stresses through the thickness of each FGM structure manufactured by DED process by using four different methods (ND, CM, DHD, and ICHD); (ii) comparison of the through-thickness stress distributions among the five different kinds of FGM specimens additively manufactured by using bidirectional, orthogonal, and island scanning strategies with the different number of interlayers; and (iii) variations of the properties such as thermal

expansion coefficient, hardness and grain microstructure in the FGM parts as well as (iv) the distribution of the bulk defects inside the FGM parts using neutron tomography.

2. Additive manufacturing, Microstructure, and Thermo-mechanical Properties

As-received commercial austenitic stainless steel powder (316L, 17Cr, 12Ni, 2.5Mo, 0.03C, 0.75Si, 2.0Mn, 0.05P and balance Fe, in wt.%) and ferritic carbon steel powder (P21, 0.2C, 0.3Si, 0.3Mn, 0.03P and balance Fe in wt.%) were prepared with the particle size of 45-150 μm as summarized in Table 1. Rectangular shape (60-mm long by 20-mm wide by 15-mm thick) of specimens were additively manufactured by using DED process on a ferritic steel substrate (S45C) with the dimension of 60-mm long by 50-mm wide by 5-mm thick plate type, Fig. 1. Denoted the longitudinal (x), transverse (y), and normal (building, z) directions. The centerline is marked along the mid-length and width through the thickness of the specimen in Fig. 1a. The DED process was performed using the laser power of 200-1000 W, a scanning speed of 14.1 mm/s, a layer thickness of 250 μm, and a hatch spacing (laser beam spot size) of 400 μm under argon gas atmosphere with a pressure of 10 mbar and an oxygen of 0.2%. In order to maintain the layer thickness and hatch width of the deposition, the laser power was changed instantly by means of automatic feedback controlling system in a DED system (INSSTEK MX-400).

A total of five cases in DED FGM were fabricated by; (*Case 1*) bidirectional scan, which is a zigzag way starting from the same location among layers and creates two parts (each part with 100 wt.% ferritic and austenitic steel compositions), Fig. 1a, (*Case 2*) bidirectional scan for three parts (two parts are same with *Case 1* and one intermediate part of 50% ferritic and 50% austenitic steel composition), Fig. 1b, (*Case 3*) bidirectional scan for five parts (two parts are same with *Case 1* and three intermediate parts processed by reducing 25% volume of the stainless steel powder sequentially from the top), Fig. 1c, (*Case 4*) orthogonal scan for

five parts (compositions of each part are same with *Case 3*), which is firstly scanned with vector along x and secondly along y starting from the same location among layers, Fig. 1d, and (*Case 5*) island scans for five parts (compositions of each part are same with *Case 3*), Fig. 1e. The island size of 5 x 5 mm^2 was deposited by the orthogonal manner without shifts or rotations between layers to eliminate any possible geometric complexity on residual stresses. Three samples were fabricated in each case using identical processing conditions and provided for residual stress measurements using ND, CM, and DHD (ICHD), respectively, Fig. 2.

Microstructural characterization was performed on cross-sections of each specimen. The specimens for optical microscopy (OM) were prepared by cutting with electrical discharging machining (EDM) and electrolytically etching them with the etchant of 10% perchloric acid and 90% acetic acid. A field-emission scanning electron microscope (JSM-7100F) equipped with electron backscatter diffraction (EBSD) system was utilized to analyze grain structure on the cross-section (y-z plane) with the step sizes of 0.5 μm in representative interface regions.

Fig. 3 shows a composite picture of the cross-sectional micrographs in each case. Firstly, it shows clear interfaces between parts and the shape of the melt pools resembles a localized puddle (equiaxed grain structure), which is explained by re-melting of a previously deposited layer by the consecutive one causing epitaxial grain growth along the building (z) direction [4,29]. The average grain size of the stainless steel part (~300 μm) is relatively larger than that of the ferritic steel part (~190 μm) macroscopically by OM as marked in Fig. 3a. Comparatively short (along x) and deep (along z) melting pool with equiaxed grains is known to be typical in DED [1.6]. It is because of the relatively higher heat input (generally laser power of kW) in DED contrast to lower heat input (~ a few hundreds W) resulting in the typical columnar grain growth structures in PBF [12]. Besides, the ferritic steel contained

parts, Fig. 3a-c, preferentially exhibit inclined equiaxed grains, which are rotated along the x axis due to the temperature gradients affecting the curvature of the solidification interface [3].

Secondly, Fig. 4 (middle) shows EBSD results of the interface taken from the marked macroscopic cross-sections (Fig. 4, top). It clearly shows the severe changes of the grain size between the ferritic and austenitic steel parts across the interface. For example, in the EBSD of *Case 1*, Fig. 4a, the average grain size near the interface was about 50 μm for the austenitic steel part and ~18 μm for the ferritic steel part as obtained by the linear intercept method. Since the cooling rate is one of the critical factors to determine the grain size, three times lower thermal conductivity of the austenitic steel (16 W/mK) than ferritic steel (43 W/mK) can lead to slower cooling and longer growth time resulting in the larger grain size of the austenitic steel part. The difference of grain size is similar when the scanning strategies is orthogonal (*Case 4*) or island (*Case 5*), as shown in Fig. 4d-e.

Noticeable macroscopic pores and defects marked in Fig. 3e and Fig. 4e (top) were further examined three dimensionally by using the DINGO neutron imaging instrument at ANSTO [37]. High spatial resolution configuration (ratio of collimator-detector length to collimator aperture equals to 1000), corresponding to a pixel size of 27 μm, was used to detect the structural defect features inside the DED FGM specimens. Projections were obtained by rotating the sample around its vertical axis (z) for 1200 angles with an equiangular spaced step of 0.3° from 0° to 360°. At each step the specimen was exposed to the neutron beam for a period of 50 seconds. The portion of the beam transmitted through the sample is converted into visible light by a 50 μm thick ^{6}LiF/ZnS scintillator and guided via a mirror to an Andor DW434 CCD camera with 2048×2028 pixels. The data sets were reconstructed with the Octopus package and visualized by AVISO 9.1 [38].

Vickers microhardness was examined across the cross-section with the step size of 0.3 mm and indentation load of 1.96 N for 10 seconds. Figure 4 (bottom) clearly shows that the micro

hardness is different among parts and the distribution is inhomogeneous within the individual layer. The hardness values ranged about 200 Hv in ferritic and austenitic steel parts increase up to 440 Hv in the interlayers. The reason is likely due to the finer grain size of the equiaxed grain structures in the gradient regions of the DED FGM structures that also can be directly shown by the EBSD results, Fig. 4 (middle) [27,29]. Two miniaturized tensile specimens (the total length of 18 mm) were prepared from each ferritic and austenitic steel parts and uniaxial tensile testing was performed at room temperature under the initial strain rate of 10^{-3} s^{-1}. The dimension of the parallel gauge was 10 mm long, 2 mm wide, and 1 mm thick. The yield strength and elongation were obtained as 1050 MPa, 0.18 for the ferritic steel and 510 MPa, 0.33 for the austenitic steel DED FGM parts, respectively.

Phase analysis was performed using x-ray diffraction. Fig. 5 shows the diffraction peaks measured at five inter-parts in *Case 3*. Other cases are similar in each part (not shown). It shows that the fcc phase in the part 1 (top layer) changes gradually to the bcc phase in the part 5, which is close to the bcc phase of the substrate. The whole peak fitting by Rietveld refinement method provides the volume fraction of the bcc phase as 0, 0.194, 0.483, 0.788, and 1.0 from part 1 to 5, respectively.

Thermal dilation experiments were performed to measure the coefficient of thermal expansion (CTE, $x10^{-6}$ /°C). The CTE sample was 30 mm long bar type with the diameter of 3 mm, which was cut by EDM from the five parts of the DED FGM in *Case 3*. Thermal expansion and contraction were recorded during heating to 1000 °C at a rate of 1 °C/s, holding for 5 min, and cooling down to room temperature at a rate of 1 °C/s.

3. Residual stress measurements

3.1. Neutron diffraction

Spatially-resolved neutron strain mapping was performed by using the KOWARI engineering strain diffractometer at ANSTO [39]. The wavelengths of 1.52 Å and 1.67 Å were selected for the diffraction planes of (311) in fcc austenitic stainless steel and (211) in bcc ferritic steel phases at scattering angles of 89.0^{o} and 91.2^{o}, respectively. Si (400) monochromator at take-off angles of 75.9^{o} and 68.0° was used to produce neutrons with these wavelengths. The scattering gauge volume of the neutron beam was defined by 2 mm wide and 15 mm high input slits and a 2 mm output slit. Thus, the nominal scattering volumes of 15(x) × 2(y) × 2(z) mm^3 (mode I) was used for collecting the diffraction patterns and strain profiles through thickness of the samples. Three normal directions, x, y and z, were measured using the gauge volume. In general, the elongated gauge volume (15 mm along in the x direction) has been accepted not to cause any potential bias due to the trivial strain gradient along the x direction [32,34].

Additional longitudinal and normal strain component measurements were carried out with 2 mm size cube gauge volume using the Residual Stress Instrument (RSI) at High-flux Advanced Neutron Application Reactor, KAERI [34]. Thus, higher spatial resolution were utilized with the gauge volume of 2(x) × 2(y) × 2(z) mm^3 (mode II). The Si (220) monochromators at take-off angles 45^{o} produced neutrons with the wavelength of 1.46 Å for the diffraction planes (311) in fcc and (211) in bcc at scattering angles of 84.4^{o} and 76.2^{o}, respectively. A total of 12 points were measured through the thickness of the DED FGM specimens starting from 2 to 18.5 mm from the top surface with 1.5 mm steps along the centerline as shown in Fig. 2. Mostly, the measurement period was about 20 minutes for each strain component achieving a strain uncertainty of about ±100 με. Comb-like “stress free” reference samples were extracted along the centerline of the specimens by EDM and cut along the z direction. Thus, the comb consists of 5 mm long (x), 10 mm wide (y), and 5 mm

deep (z) coupons. The stress-free lattice spacing (d_o) was carefully measured at the same locations of the bulk specimen with the scattering volume of 2(x) × 2(y) × 2(z) mm^3.

Diffraction peak positions were analyzed using a least squares Gaussian fitting method using instrumental data analysis programs. Once the peak position was determined, the elastic lattice strains (ε) were calculated using $\varepsilon=-cot\theta(\theta-\theta_o)=(d-d_o)/d_o$, where the θ_o (d_o) and θ (d) are the diffraction angles (d-spacings) for the stress-free and stressed materials at each position, respectively [32]. The generalized Hooke's law was used to convert elastic strains (ε_x, ε_y, ε_z) to the residual stresses (σ_x, σ_y, σ_z) along the three orthogonal directions (x, y, and z) in a given plate. The (*hkl*)-dependent diffraction elastic constants (E) and Poisson's ratio (ν) were 183.5 GPa, 0.31 for E_{311} (fcc) and 225.5 GPa, 0.28 for E_{211} (bcc) [32]. The macroscopic residual stress (σ) at location (r) was derived from averaging phase-specific stress values according to the volume fraction (V_f) of the phases [32,40];

$$\sigma_i(r) = V_f^{bcc} \cdot \sigma_i^{bcc}(r) + (1 - V_f^{fcc}) \cdot \sigma_i^{fcc}(r) \quad ; (i = x,\ y,\ or\ z) \tag{1}$$

Note that the V_f^{bcc} is the bcc volume fraction from the part obtained by the x-ray diffraction as shown in Fig. 5.

3.2. Contour method and deep hole drilling

The contour method (CM) is a technique for the determination of the residual stress over a cross-section [33]. The displacements of the cut surface (the surface contour) are created as residual stresses are relaxed. The residual stresses are computed by applying the measured displacements inversely to an assumed flat surface contour using an elastic finite element model. One stress component normal to the cut surface can be reconstructed from a cut. The main experimental procedures include: (1) specimen cutting, (2) highly accurate surface

displacement measurements, and (3) data reduction and analysis. More detailed description could be found in ref. 33.

Each DED FGM specimen was cut in half at the mid-length position as shown Fig. 2. This was done by using EDM with a 100 μm diameter brass wire. To minimize cutting induced stresses, the specimen was submerged into the temperature-controlled de-ionized water and performed the ‘‘skim cut’’ with the cutting speed of 0.15 mm/min. After cutting, the normal direction (x) displacements on the cut surfaces were measured using a scanning confocal laser probe with an accuracy of ±0.02 μm. The maximum peak-to-valley range of the contour was about ±30 μm and fitted to a smooth analytical surface for stress calculation. A three-dimensional elastic finite element model in ABAQUS/Standard 6.12 meshed geometries as hexahedral elements (C3D20R) and calculates linear elastic stress to provide the stress field normal to the plane of sectioning (σ_x) in the specimen. The elastic moduli (E) and Poisson’s ratio (v) were 193 GPa, 0.3 for fcc, 207 GPa, 0.3 for bcc, and 200 GPa, 0.3 for the substrate, respectively. Note that the elastic constants for each part of the DED FGM specimen were derived by the rule-of-mixture principle accordingly to the measured phase volume fraction.

Since the DED FGM component can contains high magnitude, tri-axial residual stresses, the incremental deep hole drilling (iDHD) method was applied. Details are well described in ref. 33. In brief, the iDHD technique is an advanced DHD method by considering plastic relaxation during the trepanning process. The main difference of the iDHD is that the core (diameter of 5 mm) is extracted in incremental machining steps and the diameter of the reference hole (diameter of 1.5 mm) is measured between each increment. The iDHD technique was used for a longitudinal (σ_x) and transverse stress (σ_y) measurements with 2 mm depth step (total of 12 points) though the thickness of the DED FGM specimens in *Cases 1, 3*, and *5*. Besides, a DHD experiment was performed through the side surface at 5 mm from the

top surface at *Case 4* in Fig. 2 in order to confirm the a longitudinal (σ_x) and normal stress (σ_z) components between DHD and ND. The elastic moduli (E) and Poisson's ratio (v) are same with the contour method.

Incremental center-hole drilling (ICHD) method is a semi-invasive, mechanical strain relief technique to determine stresses near surface [36]. The ICHD procedure involves surface preparation, gauge bonding, and circuit connections. The surface firstly degreases and neutralized to remove any oxides and oils. The strain gauge rosettes of type EA-06-031RE-120 adhered with gauge elements aligned to the x and y directions. Then a quarter Wheatstone bridge circuit was formed by soldering the lead wires to the terminals of the gauge. Finally three axis drilling machine makes a small hole into the surface at the center of a strain gauge rosette and measures the relieved strains. ICHD was performed for three specimens (*Cases 1, 3,* and *5*) from the top surface up to 500 μm with incremental depth drilling in steps of 25 μm. The strains were measured by the elements of the strain gauge rosette and the residual stresses were calculated based on ASTM-E837-13a [36]. The ICHD test was performed prior to the iDHD measurements.

4. Results

4.1. Residual stresses by neutron diffraction

Fig. 6 shows the distributions of residual stresses through the thickness of the five cases of the FGM specimens manufactured by DED process. The nominal compositional ratio between the ferritic and austenitic steels was marked in each part from the top surface. The stress uncertainties were mostly less than ± 60 MPa. Firstly for the *Case 1* in Fig. 6a, the through-thickness stress profiles of the σ_x show that tensile stresses (~300 MPa) near the top surface through austenitic steel part continuously turns into compression (up to -470 MPa) at the ferritic steel part in the middle and returns to tension at the substrate bottom of the

specimen. Such stress balanced "C" shape was also investigated in the stress depth profile of σ_y with smaller magnitude than σ_x. Owing to the accumulated thermal expansion and contraction followed by non-uniform plastic flow, higher residual stresses are often found near to the top surface of multipass thick welds [34,41].

Meanwhile, *Case 2*, Fig. 6b, shows that the stress profiles significantly fluctuate demonstrating a sine-wave-like distribution through the thickness of the specimen. Such fluctuation has been suggested as a typical stress profile feature through the thickness of thick weldments in the consideration of a stress balancing mechanism of stress redistribution [42]. In particular, the σ_x and σ_y show significant changes from tension to compression (470 to -360 MPa) in the mixture part between ferritic and austenitic steels (marked by an arrow). Note that the σ_x of 470 MPa at 2 mm below the top surface corresponds to the 92% of the yield strength (510 MPa) of the DED stainless steel part. Mukherjee *et al.* [30] reported a computational result showing sharp changes of the σ_x in the interlayer of a 2.25Cr-1Mo steel/Ti-6Al-4V and an iron-nickel alloy DED dissimilar/FGM structure. Current experimental result shows that similar variations exist in the DED FGM structure. It becomes more severe in the five layered DED FGM specimen *Case 3*. Fig. 6c shows that the abrupt change from tension to compression ($\Delta\sigma = \sigma_{max} - \sigma_{min}$ = 950 MPa) occurs when across the 2nd interface from 5 to 8 mm from the top surface. When the FGM are interlayered by using orthogonal (*Case 4*) and island (*Case 5*) DED scanning strategies, the maximum-to-minimum range ($\Delta\sigma$) becomes less extremely reduced from 950 MPa to 680 MPa and 430 MPa for *Case 4* and *Case 5* as shown in Fig. 6d-e, respectively. This effect can be associated with less heat input and effective heat-flow dissipation achieved by the alternating scans and details will be discussed in section 5.1.

The stress distribution of the normal component (σ_z) is clearly different between *Cases 1* and *2*, Fig. 6a-b. In contrast to the minor fluctuation of σ_z within ±50 MPa in *Case 1*, as

marked by a dotted arrow in Fig. 6b, *Case 2* shows noticeable increase in tensile stress up to 350 MPa at the depth of 6.5 mm. In order to resolve the sampling volume issue (described in section 4.1), Fig. 6a-b compares the σ_z profiles obtained from cube gauge volume of 8 mm^3 (2x2x2, mode II) and elongated gauge volume of 60 mm^3 (2x2x15, mode I). The results confirmed similarities of the both experiments. This large σ_z is also observed over 260 MPa among other *Cases 3*, *4*, and *5* as shown in Fig. 6c-e. Besides, the neutron diffraction results (σ_x and σ_z) at 5 mm depth in *Case 4* were confirmed by the DHD analysis as marked in Fig. 6d. Thus, it is suggested that there are significant amounts of stresses along the building direction (σ_z) in the DED FGM structure. It has been mainly attributed to the thermal excursion and accumulation along the building direction during additive manufacturing and the plane stress condition ($\sigma_z = 0$) or hydrostatic stress condition ($\sigma_x \approx \sigma_y \approx \sigma_z$) is not valid in the middle of the DED and/or FGM DED structures [10,21]. Besides, it possibly assumes a presence of significant shear stress components, therefore, manifesting rotation of the principal axes of the stress tensor as a function of depth [26].

4.2. Residual stresses by contour and deep hole drilling methods

Fig. 7 shows the results from the contour method (CM) as two-dimensional maps of the σ_x. The stress uncertainty for the CM measurements was about ± 30 MPa. Through-thickness profiles were extracted from the maps along the centerlines and compared to the ND results. Firstly, the residual stress maps show clear differences among the cases. When observed the stress profiles of the *Cases 1*, *2*, and *3*, which were all processed by the same bidirectional scan as shown in Fig. 1a-c, tensile stresses near the top surface continuously change to the compression in the middle parts of the DED FGM specimens to balance the stress state (Fig. 7a-c). Considering three five-layered systems, the through-thickness stress distribution becomes relatively homogeneous in *Cases 4* and *5* when compared to *Case 3*. The extracted

by CM stress profiles show that the difference of stress values ($\Delta\sigma$) in *Cases 1*, *2*, and *3* clearly decreases when the DED scanning strategies are adopted by the orthogonal (*Case 4*) or island (*Case 5*) scans as shown in Fig. 7d-e, respectively. For example, the maximum-to-minimum difference of the stress ($\Delta\sigma_x$) decreases from 770 MPa in *Case 3* (bidirectional scan) to 450 MPa in *Case 4* as marked in Fig. 7c-d. There is minor differences in magnitude between ND and CM near the abrupt variations of the σx profile. It is likely due to the inappropriate "stress-free" ND reference specimens associated with the complex microstructural mixture between bcc ferrite and fcc austenite and/or the CM method can provoke the effects of yielding on the cut surface as high stresses are released [33,34].

Finally, Fig. 8 shows the residual stress profiles obtained from the DHD measurements along the centerline (Fig. 2) through sample thickness in *Cases 1*, *3*, and *5*. It shows fine (0.2 mm) through-depth resolution. Owing to no severe plastic relaxation of the stressed region in the whole thickness of the specimen, the iDHD results were similar to DHD results. Fig. 8 shows that the range of stress values ($\Delta\sigma$) is relatively decreased in *Case 5* when compared to *Cases 1* and *3* in both σ_x and σ_y DHD profiles. Besides, the DHD results elucidate the maximum stress location near top surface and the minimum at 8 mm depth in the mixture parts of *Cases 3* and *5* in Fig. 8b-c. Here we include neutron diffraction (ND) results and confirmed overall trends are similar between DHD and ND. There is a slight difference of less than ±100 MPa in the middle parts of the DED FGM *Case 5*, Fig. 8c. The difference was confirmed by the ND experiments measured by using higher spatial resolution (mode II) as marked ND (II). Several uncertainties have been suggested for the discrepancy including misalignment of the reference hole, calibration and curve-fitting of the air sensing probe, and material constant/microstructure effects [35,36].

5. Discussion

5.1. Through-thickness distribution of residual stresses in additive manufactured FGM

The discussion starts by examining the significant changes of the residual stress profiles in the DED FGM structure. Among *Cases 1*, *2*, and *3*, the interlayer causes sine-wave like fluctuations from tension near the top surface to compression in the 2nd or 3rd layers ($\Delta\sigma$ = 950 MPa) through the thickness of the specimens, Fig. 6a-c. Significant tensile stresses are often found along the interface between the ferritic and austenitic steel welds due to the large mismatch of the coefficient of thermal expansion (CTE, x10^{-6} /°C) of the two dissimilar materials [43]. Fig. 9 shows the CTE variations in each part of the current DED FGM specimen measured 16.3 for the stainless steel part and 12.0 for the ferritic steel part by analyzing the linear expansion from room temperature to 100 °C. It provides the CTE difference (ΔCTE) of 4.3 in the entire DED FGM structure. Although the CTE decreases with a reduction in the stainless steel composition, most of the ΔCTE (~3.1) occurs when the steel added by ~50%. Thus, it can be the reason of the significant stress difference was observed in the 2nd (*Case 2*) and 3rd (*Case 3*) parts as shown in Fig. 6b-c. Indeed, the two dimensional stress map by CM clearly shows the inhomogeneity through the thickness among the parts in *Cases 2* and *3* in Fig. 7b-c. The current ΔCTE of 3.1 can cause a mismatch in terms of thermal strain (ε^{th}) of about 4,600 με based on a simple estimation (ε^{th} = ΔCTE x ΔT), supposed that the peak temperature of the laser beam is 1500 °C and cools down to room temperature during DED process [24,30]. It is corresponding to about 930 MPa with the elastic constant of 203 GPa in the interlayer of *Case 3* and the value is comparable to the range of stress ($\Delta\sigma$ = ~950 MPa) in Fig. 6c.

Secondly, let us discuss about the influence of the scanning strategy on the residual stress distributions in the DED FGM structure. The range of stress values ($\Delta\sigma$) significantly decreases from 950 MPa (*Case 3*) to ~ 430 MPa (*Cases 4* and *5*) in Fig. 6c-e. Overall, it is consistent among ND, CM, and DHD as shown in Fig. 6-8. The reason of the significant $\Delta\sigma$

decreases is attributed to the origin of residual stresses in additive manufacturing processes, for example, the spatial temperature gradient (localized heating/cooling by the heat source), followed by thermal expansion/contraction and strain compatibility due to uneven distribution of plastic flow [3,13,23]. Thus, shorter deposition length (scanning in smaller islands) and/or less heat accumulation (orthogonal scan) strategies can mitigate residual stresses. It is explained by the less amount of heat input and moderate thermal gradients for the island scan and effective heat source dispersion along multiple directions rather than heat accumulation along the building direction for the orthogonal scan, respectively [44,45]. As a result, the island scan (*Case 5*) shows much smaller grain size compared to the bidirectional scan (*Case 3*) in Fig. 4. The bidirectional scan (*Case 3*) exhibits an oriented solidification grain structure between layers as marked by arrows in Fig. 3d, whereas the orthogonal scan (*Case 4*) has various maximum heat flow vectors oriented to different directions among layers as marked in Fig. 3d.

5.2. Residual stress distribution near surface and defects inside FGM

Since the fracture mechanics focuses on stress concentrations around localized defects and the stress-driven crack initiation and propagation, the residual stress distribution near surface has an importance for the DED FGM specimens [9,26,29]. Fig. 10 shows that the compressive stress (σ_x) of -200 MPa at 25 μm depth changes to tension reaching 300 MPa at ~200 μm and gradually decrease to -200 MPa at 500 μm in *Case 1*. It is a comparable to σ_y and other cases. A number of studies reported residual stresses near-to-surface distributions in various AM components [20,24,25,30,46]. For example, tensile stresses of 150 and 200 MPa were analyzed by x-ray diffraction in island and unidirectional scanned SLM stainless steel specimens, respectively [20,25] and over 435 MPa in unidirectional scanned SLM steel by hole drilling [46]. Meanwhile, similar to the current study, noticeable compression stresses

(ranging from -50 to -250 MPa) were simulated in a unidirectional DED stainless steel [30]. Since the SLM is typically processed with lower energy density (<100 J/mm^3 for Ti-6Al-4V) on a thin layer than DED (90-220 J/mm^3), it is suggested that the SLM leads to the fast cooling rates, higher thermal gradients, and material hardening resulting in higher tensile stresses compared to the DED in general [1].

The occurrence of macroscopic defects in the DED FGM specimen was assessed by neutron diffraction tomography with actual spatial resolution of about 50 μm. The transversal (across x) and longitudinal (along x) cross-section of the neutron tomographic reconstructions were used for the inspection of internal defects, Fig. 11. No clear defects are detectable in *Case 1* (Fig. 11a) and *Cases 2*, *3*, and *4* (not shown), while a number of defects were found in *Case 5* (Fig. 11b). Neutron tomography shows that the three dimensional distribution of defects is preferentially located along the corners of the DED islands and have an equivalent diameter (the diameter of the spherical particle of same volume) in the range of 100 - 900 μm, Fig. 11c. Porosities and lack-of-fusion voids are typical defects in AM and often reported in the case of an island scanned component [5]. Three main mechanisms are summarized for the defects: (i) entrapped vapor in the keyhole mode due to very high power intensity; (ii) captured gas during powder atomization; and (iii) lack of fusion by inadequate penetration [47]. It is suggested that the observed defects are the lack-of-fusion driven pores, Fig. 11c, which are normally formed along the corners of the previously deposited layers (marked region of interest in Fig. 11b as highlighted in Fig. 11d.

6. Conclusions

1. This paper constitutes detailed results obtained from five kinds of directed energy deposition (DED) functionally graded material (FGM) specimens. Using variable compositional ratio between ferritic and austenitic steel, two (*Case 1*), three (*Case 2*), and

five (*Case 3*) layered FGM structures were additively manufactured with bidirectional scanning on a steel substrate using DED process. Two more specimens were prepared by the orthogonal (*Case 4*) and island (*Case 5*) scanning strategies in each layer for comparison. Microstructure, thermal, mechanical properties, and residual stresses were examined through the thickness of the DED FGM specimens.

2. Distinct microstructural features were investigated in the ferritic and austenitic steel DED FGM parts. Both parts show an equiaxed grain structure created by the epitaxial grain growth along the building direction (z). The ferritic steel part shows preferentially inclined grain structure in the bidirectional scan (*Cases 1*, *2*, and *3*), whiles it becomes less preferred in the orthogonal (*Case 4*) and island scan (*Case 5*) due to the mixture of the scanning strategies among interlayers. The austenitic steel part shows much larger grain size (~300 μm) compared to the ferritic steel part (~190 μm). Furthermore, the interface characterization by EBSD confirms significant decreases of the grain size when across from the austenitic to the ferritic steel parts. Besides, island scanning build-up (*Case 5*) leads to further smaller grain size (~60 μm) than the bidirectional scan (~110 μm) near the interface of the DED FGM components.

3. The yield strength and elongation were determined as 510 MPa, 0.33 for the austenitic steel part and 1050 MPa, 0.18 for the ferritic steel part of the FGM DED specimen, respectively. The hardness of about 200 Hv in the steel (or stainless steel) part increases up to 440 Hv in the mixed parts as the grain size decreases. The coefficient of thermal expansion (CTE, $x10^{-6}$/°C) decreases from 16.3 to 12.0 as the composition changes from the austenitic to ferritic steel parts. Most of the CTE difference (ΔCTE) of ~3.1 occurs when the ferritic steel phase added by ~50% in the DED FGM part.

4. Neutron diffraction (ND), contour method (CM), deep hole drilling (DHD), and incremental center-hole drilling (ICHD) were applied to obtain full-field knowledge of the magnitudes and spatial distributions of the residual stresses through the thickness of the DED FGM structures.

- From the top of the specimen, near-surface stresses were investigated by ICHD technique and compressive stresses (σ_x and σ_y) of about -200 MPa were found at 25 μm depth. The compressive stress changes to tension of approximately 300 MPa magnitude at 200 μm depth. Then, it reaches tension of 410 MPa (~80% of yield strength) at 2 mm depth and significantly changes from tension to compression (up to 950 MPa) as a sine-wave stress profile analyzed by DHD and ND in *Cases 1*, *2*, and *3*.
- The range of stress values ($\Delta\sigma$) is alleviated to 680 MPa when the FGM are interlayered with the orthogonal scan (*Case 4*) and further reduced to 430 MPa for the island scan (*Case 5*). It is consistent with the two dimensional stress mapping results of CM. It concludes that the large $\Delta\sigma$ observed in the bidirectional can be significantly reduced when orthogonal or island DED scanning strategies are adopted.
- There is a significant amount of the normal stress (σ_z) along the building direction in the DED FGM structure. Both ND and DHD measurements confirm strong tension up to 350 MPa at 6.5 mm depth.

5. Island scanning strategy without shift and rotation between layers causes a number of internal defects in the DED FGM specimen. Neutron tomography shows that the defects have an equivalent diameters of 100 to 900 μm and located along the corner junctions of the interfacing islands. The main cause of porosities is suggested to be the lack-of-fusion defects by inadequate penetration along the edge of the previously deposited layer. Meanwhile, no

clear macroscopic defects were investigated in the case of the bidirectional and orthogonal scanning cases.

6. Current systematic studies conclude that the scanning strategy is effective to diminish the maximum tensile stress in the DED processed ferrite and austenite FGM component. Compared to the significant amounts of residual stresses up to 470 MPa (92% of yield strength) of the bidirectional scan, the orthogonal and island scans considerably reduce the maximum longitudinal stress to 365 and 260 MPa, respectively. Furthermore, the chemically mixed interlayers within the FGM structure can modify the shape of the profile. The range of stress value ($\Delta\sigma$) fluctuating up to 950 in the bidirectional scanned specimen was reduced to 55% and 28% of the $\Delta\sigma$ when processed by the orthogonal and island scans, respectively.

Acknowledgements

This work was supported by the National Research Foundation of Korea (NRF) grant funded by the Korean government (No. NRF-2017M2A2A6A05017653) and the Australian Nuclear Science and Technology Organization (neutron proposal P5085).

References

[1] D. Herzog, V. Seyda, E. Wycisk, C. Emmelmann, Additive manufacturing of metals, Acta Mater. 117 (2016) 371-392.

[2] W.J. Sames, F.A. List, S. Pannala, R.R. Dehoff, S.S. Babu, The metallurgy and processing science of metal additive manufacturing, Inter. Mater. Reviews 61 (2016) 315-360.

[3] T. DebRoy, H.L. Wei, J.S. Zuback, T. Mukherjee, J.W. Elmer, J.O. Milewski, A.M. Beese, A. Wilson-Heid, A. De, W. Zhang, Additive manufacturing of metallic components – process, structure and properties, Prog. Mater. Sci. 92 (2018) 112-224.

[4] A. Haider, G. Hassan, M. Kamran, Effect of scanning strategies on residual stress and mechanical properties of Selective Laser Melted Ti6Al4V, Mater. Sci. Eng. A (2018) 175-187.

[5] L. Thijs, K. Kempen, J.-P. Kruth, J.V. Humbeeck, Fine-structured aluminium products with controllable texture by selective laser melting of pre-alloyed AlSi10Mg powder, Acta Mater. 61 (2013) 1809-1819.

[6] N. Raghavan, R. Dehoff, S. Pannala, S. Simunovic, M. Kirka, J. Turner, N. Carlson, S.S. Babu, Numerical modeling of heat-transfer and the influence of process parameters on tailoring the grain morphology of IN718 in electron beam additive manufacturing, Acta Mater. 112 (2016) 303-314.

[7] Z.H. Liu, D.Q. Zhang, S.L. Sing, C.K Chua, L.E. Loh, Interfacial characterization of SLM parts in multi-material processing: Metallurgical diffusion between 316L stainless steel and C18400 copper alloy, Mater. Char. 94 (2014) 116-125.

[8] K.G. Prashanth, S. Scudino, J. Eckert, Defining the tensile properties of Al-12Si parts produced by selective laser melting, Acta Mater. 126 (2017) 25-35.

[9] A. Riemer, S. Leuders, M. Thöne, H.A. Richard, T. Tröster, T. Niendorf, On the fatigue crack growth behavior in 316L stainless steel manufactured by selective laser melting, Eng. Frac. Mech. 120 (2014) 15-25.

[10] P. Rangaswamy, M.L. Griffith, M.B. Prime, T.M. Holden, R.B. Rogge, J.M. Edwards, R.J. Sebring, Residual stresses in LENS components using neutron diffraction and contour method, Mater. Sci. Eng. A 339 (2005) 72-83.

[11] M.F. Zaeh, G. Branner, Investigation on residual stress and deformation in selective laser melting, Prod. Eng. Res. Devel. 4 (2010) 35-45.

[12] A.S. Wu, D.W. Brown, M. Kumar, G.F. Gallegos, W.E. King, An experimental investigation into additive manufacturing-induced residal stresses in 316L stainless steel, Matall. Mater. Trans. A 45 (2014) 6260-6270.

[13] N. Nadammal, S. Cabeza, T. Mishurova, T. Thiede, A. Kromm, C. Seyfert, L. Farahbod, C. Haberland, J.A. Schneider, P.D. Portella, G. Bruno, Effect of hatch length on the development of microstructure, texture and residual stresses in selective laser melted superalloy Inconel 718, Mater. Deg. 134 (2017) 139-150.

[14] L.M. Sochalski-Kolbus, E.A. Payzant,P.A. Cornwell, T.R. Watkins, S.S. Babu, R.R. Dehoff, M. Lorzenz, O. Ovchinnikova, C. Duty, Comparison of residual stresses in Inconel 718 simple parts made by electron beam melting and direct laser metla sintering, Matall. Mater. Trans. A, 46 (2015) 1419-1432.

[15] B.A. Szost, S. Terzi, F. Martina, D. Boisselier, A. Prytuliak, T. Pirling, M. Hofmann, D.J. Jarvis, A comparative study of additive manufacturing techniques: Residual stress and microstructural analysis of CLAD and WAAM printed Ti-6Al-4V components, Mater. Deg. 89 (2016) 559-567.

[16] Z. Wang, E. Denlinger, P. Michaleris, A.D. Stoica, D. Ma, A.M. Beese AM, Residual stress mapping in Inconel 625 fabricated through additive manufacturing: Method for neutron diffraction measurements to validate thermomechanical model predictions, Mater. Deg. 113 (2017) 169-177.

[17] K. An, L. Yuan, L. Dial, I Spinelli, A.D. Stoica, Y. Gao, Neutron residual stress measurement and numerical modeling in a curved thin-walled structure by laser powder bed fusion additive manufacturing, Mater. Deg. 135 (2017) 122-132.

[18] Z. Wang, A.D. Stoica, D. Ma, A.M. Beese, Stress relaxation in a nickel-base superalloy at elevated temperatures with in situ neutron diffraction characterization: Application to additive manufacturing, Mater. Sci. Eng. A, 714 (2018) 75-83.

[19] Y. Liu, Y. Yang, D. Wang, A study on the residual stress during selective laser melting (SLM) of metallic powder, Int. J. Adv. Manuf. Technol. 87 (2016) 647-656.

[20] T. Simson, A. Emmel, A. Dwars, J. Böhm, Residual stress measurements on AISI 316L samples manufactured by selective laser melting, Additive Manuf. 17 (2017) 183-189.

[21] R.J. Moat, A.J. Pinkerton, L. Li, P.J. Withers, M. Preuss, Residual stresses in laser direct metal deposited Waspaloy, Mater. Sci. Eng. A, 528 (2011) 2288-2298.

[22] B. Vrancken, V. Cain, R. Knutsen, J.V. Humbeeck, Residual stress via the contour method in compact tension specimens produced via selected laser melting, Scripta Mater. 87 (2014) 29-32.

[23] E.R. Denlinger, J.C. Heigel, P. Michaleris, T.A. Palmer, Effect of inter-layer dwell time on distorsion and residual stress in additive manufacturing of titanium and nickel alloys, J. Mater. Proces. Technol. 215 (2015) 123-131.

[24] Y.P. Yang, M. Jamshidinia, P. Boulware, S.M. Kelly, Prediction of microstructure, residual stress, and deformation in laser powder bed fusion process, Comp. Mech. 61 (2018) 61, 599-615.

[25] O. Fergani, F. Berto, T. Welo, S.Y. Liang, Alalytical modeling of resiudal stress in additive manufacturing, Fat. Frac. Eng. Mater. Struc. 40 (2017) 971-978.

[26] T. Mukherjee, W. Zhang, T. DebRoy, An improved prediction of residual stresses and distortion in additive manufacturing, Comp. Mater. Sci. 126 (2017) 360-372.

[27] B.E. Carroll, R.A. Otis, J.P. Borgonia, J. Suh, R.P. Dillon, A.A. Shapiro, D.C. Hofmann, Z.-K. Liu, A.M. Beese, Functionally graded material of 304L stainless steel and inconel 625 fabricated by directed energy deposition: Characterization and thermodynamic modeling, Acta Mater. 108 (2016) 46-54.

[28] L.D. Bobbio, R.A. Otis, J.P. Borgonia, R.P. Dillon, A.A. Shapiro, Z.-K. Liu, A.M. Beese, Additive manufacturing of a functionally graded material from Ti-6Al-4V to Invar:

Experimental characterization and thermodynamic calculations, Acta Mater. 127 (2017) 133-142.

[29] V.A. Popovich, E.V. Borisov, A.A. Popovich, V.Sh. Sufiiarov, D.V. Masaylo, L. Alzina, Functionally graded Inconel 718 processed by additive manufacturing: Crystallographic texture, anisotropy of microstructure and mechanical properties, Mater. Des. 114 (2017) 441-149.

[30] T. Mukherjee, J.S. Zuback, W. Zhang, T. DebRoy, Residual stresses and distorsion in additively manufactured compositionally graded and dissimilar joints, Comp. Mater. Sci. 143 (2018) 325-337.

[31] A.J. Allen, M.T. Hutchings, C.G. Winsor, C. Andreani, Neutron diffraction methods for the study of residual stress fields, Adv. Phys. 34 (1985) 445-473.

[32] M.T. Hutchings, P.J. Withers, T.M. Holden, T. Lorentzen, Introduction to the Characterization of Residual Stress by Neutron Diffraction, first ed., Taylor and Francis, London, 2005.

[33] M.B. Prime, Cross-sectional mapping of residual stresses by measuring the surface contour after a cut, J. Eng. Mater. Tech. Trans. ASME, 123 (2001) 162-168.

[34] W. Woo, G.B. An, E.J. Kingston, A.T. DeWald, D.J. Smith, M.R. Hill, Through-thickness distributions of residual stresses in two extreme heat-input thick welds: A neutron diffraction, contour method and deep hole drilling study, Acta Mater. 61 (2013) 3564-3574.

[35] D.M. Goudar, C.E. Truman, D.J. Smith, Evaluating uncertainty in residual stress measured using the deep-hole drilling technique, Strain, 47 (2011) 62-74.

[36] D. George, E. Kingston, D.J. Smith, Measurement of through-thickness stresses using small holes, J. Strain. Anal. Eng. Des. 37 (2002) 125-139.

[37] U. Garbe, T. Randall, C. Hughes, G. Davidson, S. Pangelis, S. Kennedy, A New Neutron Radiography/Tomography/Imaging Station DINGO at OPAL, Physics Procedia. 69 (2015) 27-32.

[38] M. Dierick, B. Masschaele, L. Van Hoorebeke, Octopus, a fast and user-friendly tomographic reconstruction package developed in LabView, Meas. Sci. Tech. 15 (2004) 1366-1370.

[39] A. Brule, O. Kristein, Residual stress diffractometer KOWARI at the Australian research reactor OPAL: Status of the project, Physica B: Condensed Matter. 385-386 (2006) 1040-1042.

[40] V. Luzin, K. Thorogood, J.R. Griffiths, C.J. Davidson, T.R. Finlayson, Residual stress in metal-matrix composite cylinder measured by neutron diffraction and contour method residual stresses, in ICRS-10 Materials Research Forum, Materials Research Proc. (2016) 401-406.

[41] D.J. Smith, P.J. Bouchard, D. George, Measurement and prediction of residual stresses in thick-section steel welds, J. Strain Anal. Eng. Deg. 35 (2000) 287-305.

[42] K. Masubuchi, Analysis of welded structures, first ed., Pergamon, New York, 1980, Ch. 6. Distribution of residual stresses in weldments, pp. 225-232.

[43] W. Woo, G.B. An, C.E. Truman, W. Jiang, M.R. Hill, Two-dimensional mapping of residual stresses in a thick dissimilar weld using contour method, deep hole drilling, and neutron diffraction, J. Mater. Sci. 51 (2016) 10620-10631.

[44] M. Gao, Z. Wang Z, X. Li, X. Zeng, The effect of deposition patterns on the deformation if substrates during direct laser fabrication, J. Eng. Mater. Tech. 135 (2013) 034502.

[45] H.L. Wei, J. Mazumder, T. DebRoy, Evolution of solidification texture during additive manufacturing, Scientific Report, 5 (2015) 16446.

[46] C. Casavola, S.L. Campanelli, C. Pappalettere, Preliminary investigation on distribution of residual stress generated by the selective laser melting process, J. Strain Analysis, 44 (2009) 93-104.

[47] K. Darvish, Z.W. Chen, T. Pasang, Reducing lack of fusion during selective laser melting of CoCrMo alloy: Effect of laser power on geometrical features of tracks, Mater. Des. 112 (2016) 357-366.

Figure captions

Fig. 1. Schematic of the sample dimension and scanning strategies in additive manufactured functionally graded material (FGM) structures: (a) *Case 1*, bidirectional scan in two parts, (b) *Case 2*, bidirectional scan in three parts, (c) *Case 3*, bidirectional scan in five parts, (d) *Case 4*, orthogonal scan in five parts, and (e) *Case 5*, island scan in five parts.

Fig. 2. Measurement locations. Contour in the cut surface, macroscopic stress-free coupon, and the reference core were shown for the contour method (CM), neutron diffraction (ND), and deep hole drilling (DHD), respectively.

Fig. 3. Cross-sectional macrostructure of the direct energy deposition (DED) functionally graded material (FGM) specimens: (a) *Case 1*, (b) *Case 2*, (c) *Case 3*, (d) *Case 4*, and (e) *Case 5*.

Fig. 4. Optical macrographs taken at the cross-section (top), electron backscatter diffraction (EBSD) images at the interfaces marked as squares in the macrographs (middle), and microhardness profiles along the centerline (dot line) and hardness mapping at the cross-section (dot square) in each case (bottom).

Fig. 5. Phase analysis using x-ray diffraction. The diffraction peaks measured at the five inter-parts and substrate in *Case 3*.

Fig. 6. Residual stresses through the thickness of the DED FGM specimens along the centerline by neutron diffraction: (a) *Case 1*, (b) *Case 2*, (c) *Case 3*, (d) *Case 4*, and (e) *Case*

5. The normal stress component (σ_z) was measured with two spatial resolutions (scattering volume of 60 mm^3 in mode I, and 8 mm^3 in mode II). Deep hole drilling results of the longitudinal (σ_x) and normal (σ_z) stress components were marked in (d) *Case 4*.

Fig. 7. Two-dimensional mapping of the longitudinal residual stress (σ_x) constructed by contour method (CM). Through-thickness stress profiles by CM were shown and compared to the neutron diffraction: (a) *Case 1*, (b) *Case 2*, (c) *Case 3*, (d) *Case 4*, and (e) *Case 5*.

Fig. 8. Through-thickness distributions of the longitudinal (σ_x) and transverse (σ_y) stresses using the deep hole drilling (DHD) and incremental DHD (iDHD): σ_x in (a) *Case 1*, (b) *Case 3*, (c) *Case 5*, and σ_y in (d) *Case 1*, (e) *Case 3*, (f) *Case 5*. For comparison neutron diffraction (ND) results were marked. Note that the σ_x in (c) *Case 5* was measured with two spatial resolutions, scattering volume of 60 mm^3 as ND (I) and 8 mm^3 as ND (II).

Fig. 9. The coefficient of thermal expansion (CTE, $x10^{-6}$, 1/°C) in the substrate and different parts of the DED FGM specimen.

Fig. 10. Near surface (up to 0.5 mm) distributions of the longitudinal (σ_x) and transverse (σ_y) stresses in *Cases 1*, *3*, and *5* using the incremental center-hole drilling (ICHD) method.

Fig. 11. Neutron tomographic images: transversal (across x) and longitudinal (along x) cross sections of (a) *Case 1* and (b) *Case 5*. (c) Three-dimensional map of porosities of *Case 5*; the color code adopted to render the volume of the pores is indicated by the chart on the right-bottom side. (d) defects investigation in the region of interest (ROI) marked with a red

rectangle in (b). The borders of ROI are defined by dotted lines; the pores are highlighted with blues circle, while the cracks are signaled with red arrows.

FIGURE 1

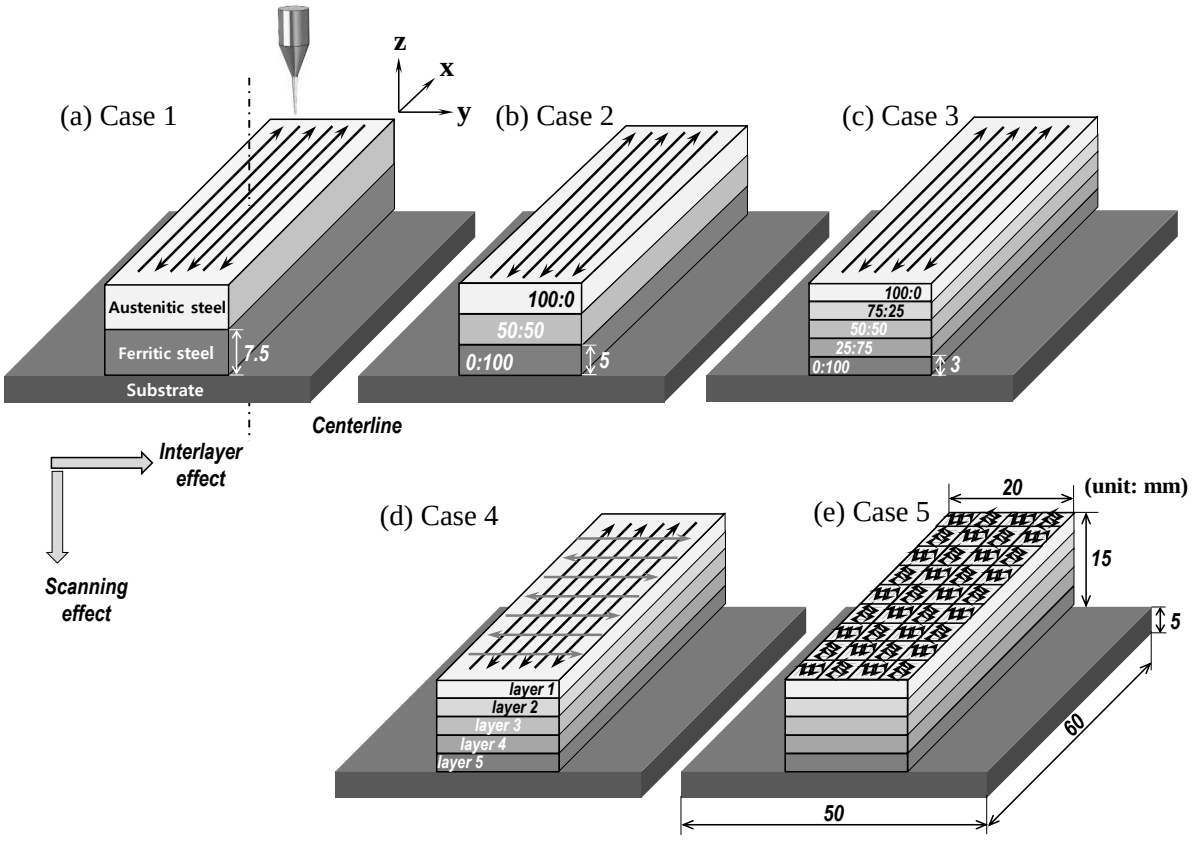
z
x
y
(a) Case 1
(b) Case 2
(c) Case 3
Austenitic steel
Ferritic steel
7.5
Substrate
100:0
50:50
0:100
5
100:0
75:25
50:50
25:75
0:100
3
Centerline
Interlayer effect
Scanning effect
(d) Case 4
(e) Case 5
(unit: mm)
20
15
5
layer 1
layer 2
layer 3
layer 4
layer 5
60
50

FIGURE 2

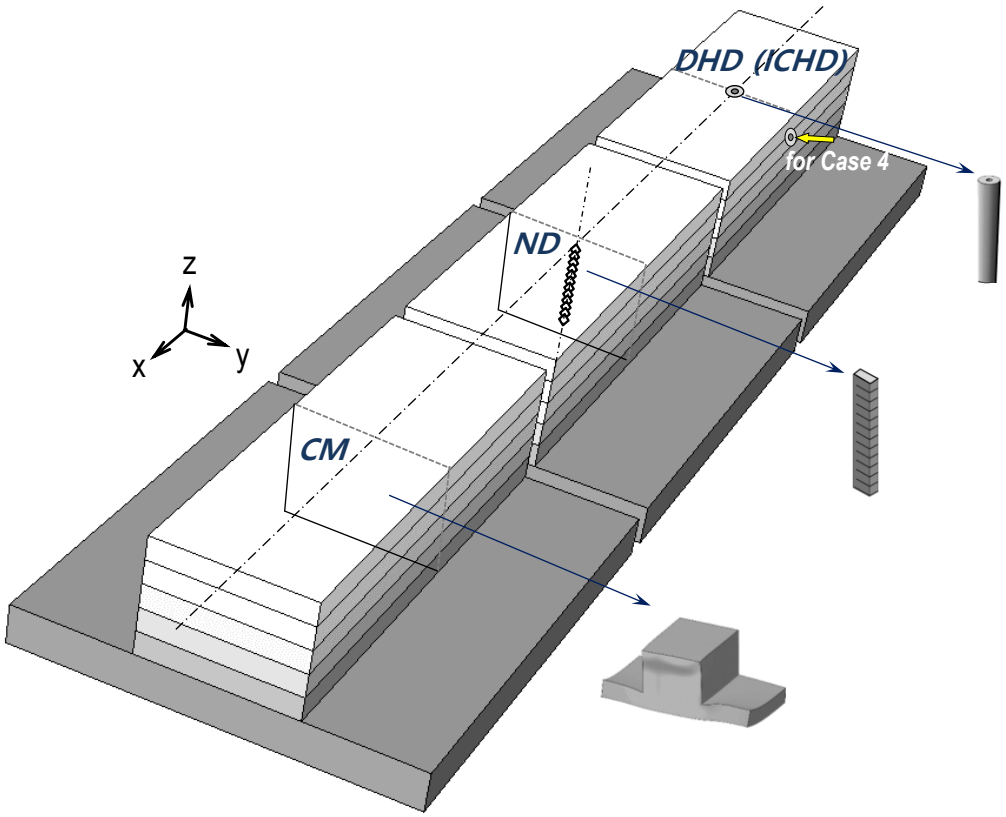

FIGURE 3

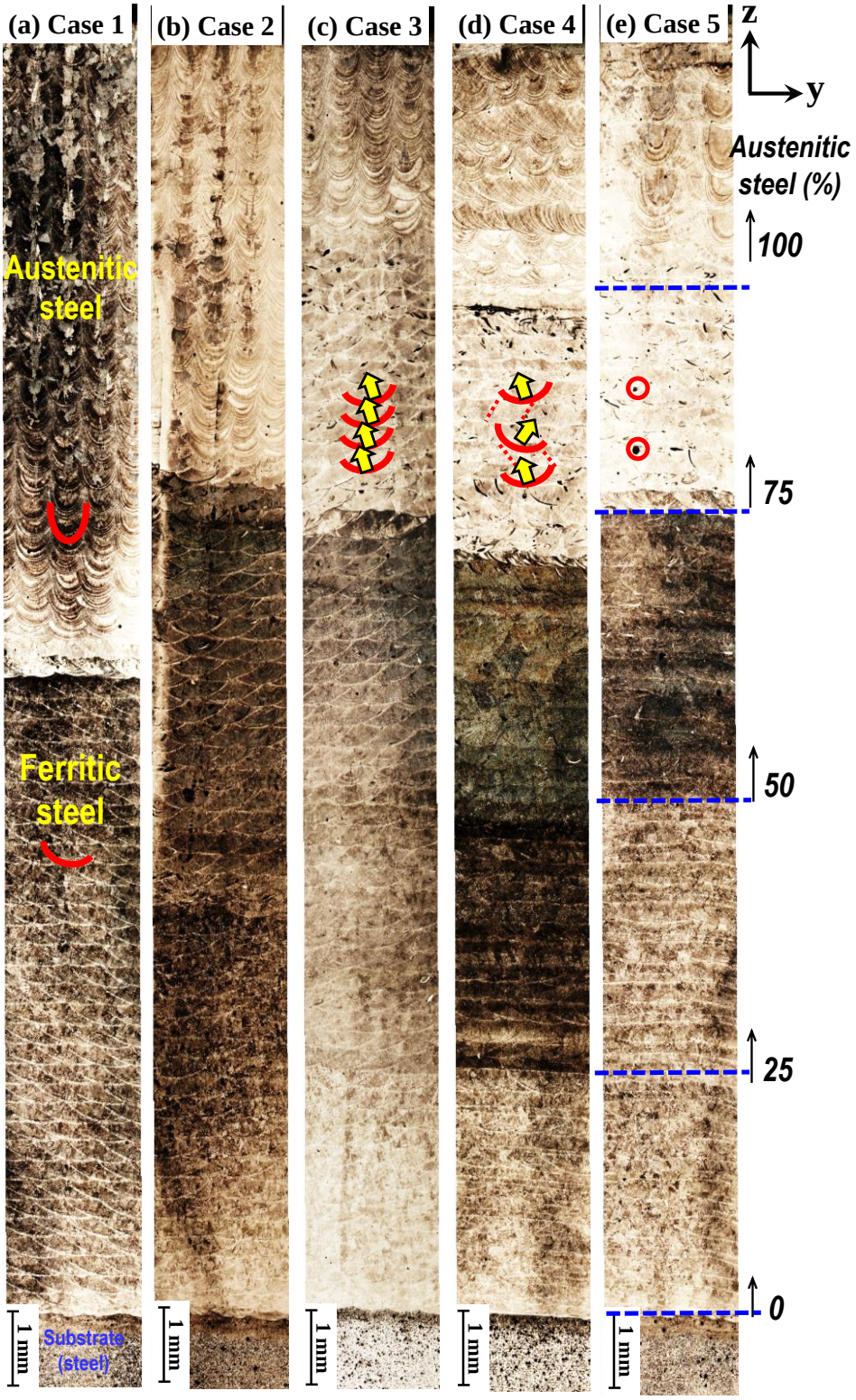
(a) Case 1
(b) Case 2
(c) Case 3
(d) Case 4
(e) Case 5
z
y
Austenitic steel (%)
100
75
50
25
0
Austenitic steel
Ferritic steel
1 mm
Substrate (steel)

FIGURE 4

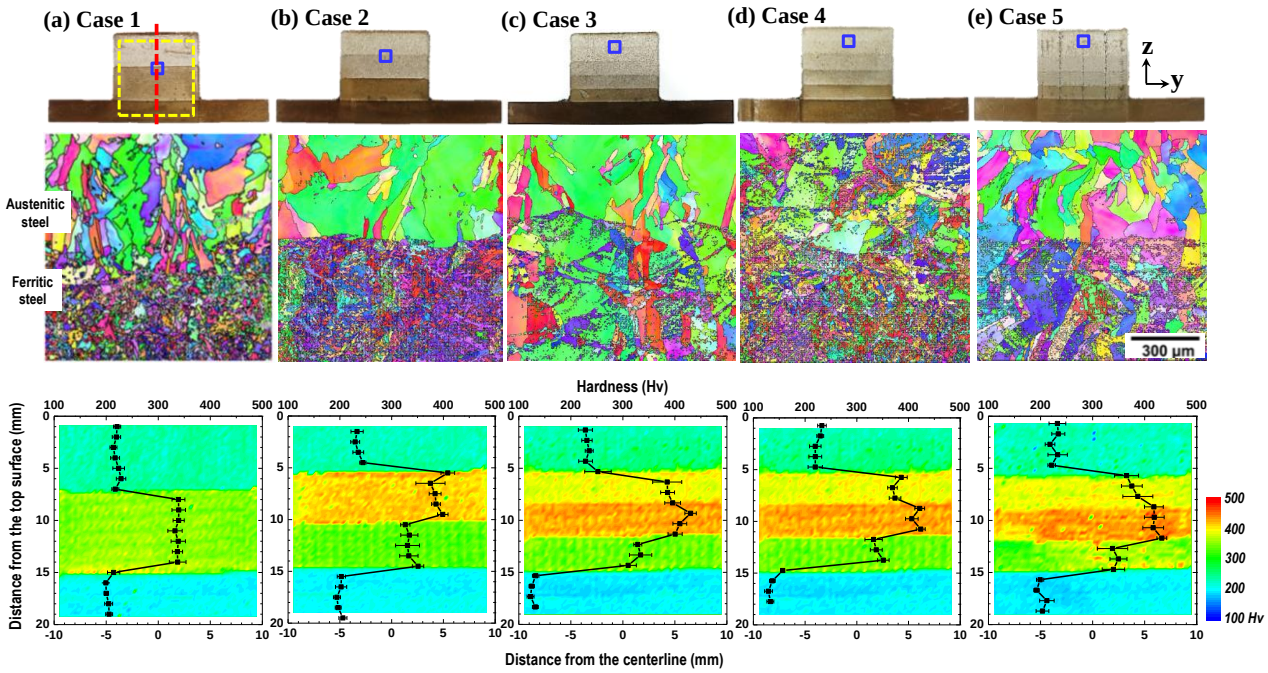
(a) Case 1
(b) Case 2
(c) Case 3
(d) Case 4
(e) Case 5
z
y
Austenitic steel
Ferritic steel
300 µm
Hardness (Hv)
Distance from the top surface (mm)
Distance from the centerline (mm)
100 Hv

FIGURE 5

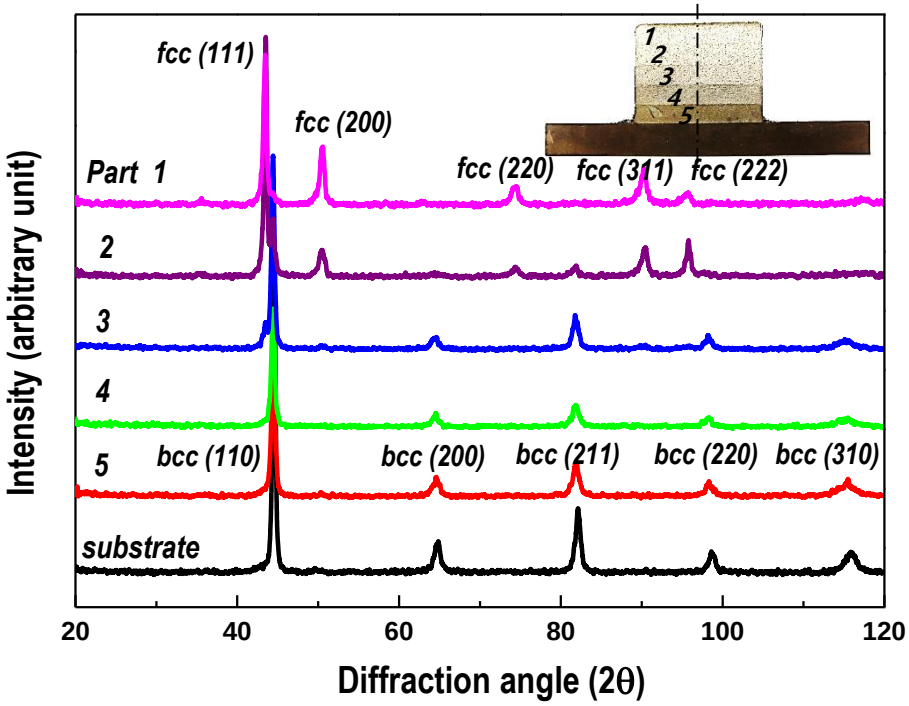
fcc (111)
fcc (200)
fcc (220)
fcc (311)
fcc (222)
Part 1
2
3
4
5
bcc (110)
bcc (200)
bcc (211)
bcc (220)
bcc (310)
substrate
1
2
3
4
5
Intensity (arbitrary unit)
20
40
60
80
100
120
Diffraction angle (2θ)

FIGURE 6

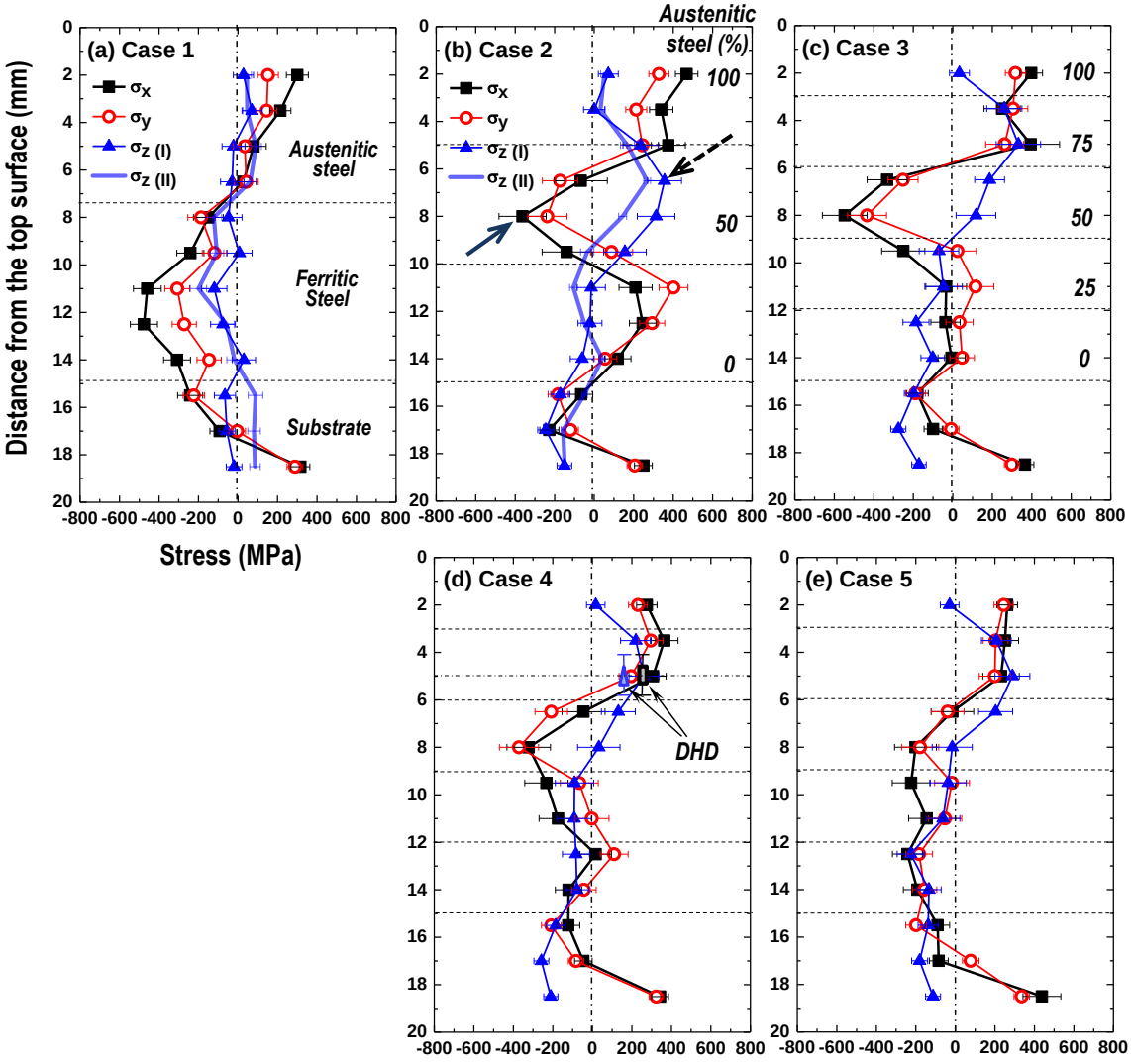
(a) Case 1
(b) Case 2
(c) Case 3
(d) Case 4
(e) Case 5
σx
σy
σz (I)
σz (II)
Austenitic steel
Ferritic Steel
Substrate
Austenitic steel (%)
100
75
50
25
0
DHD
Distance from the top surface (mm)
Stress (MPa)

FIGURE 7

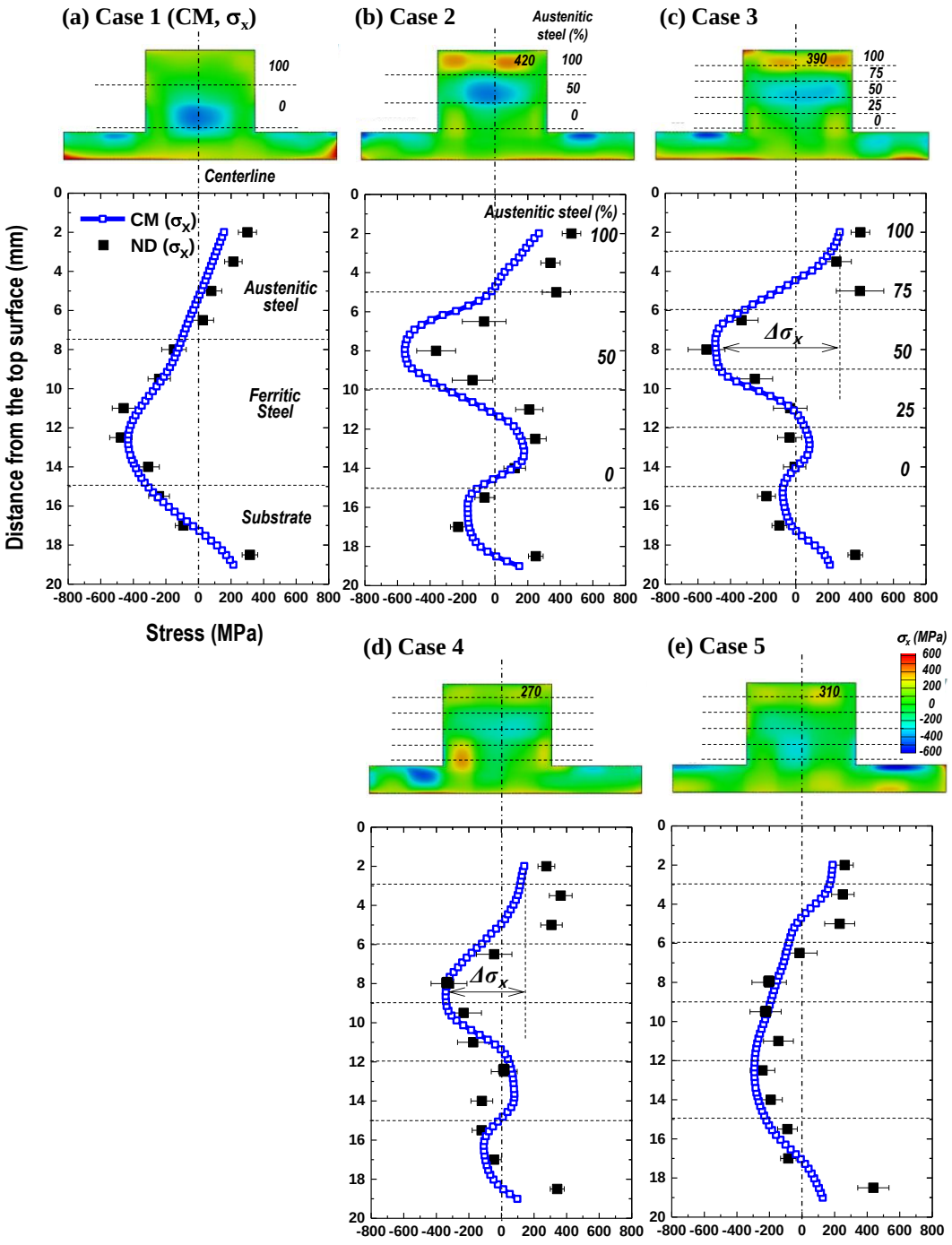
(a) Case 1 (CM, σx)
(b) Case 2
(c) Case 3
Austenitic steel (%)
100
0
420
390
75
50
25
Centerline
CM (σx)
ND (σx)
Austenitic steel
Ferritic Steel
Substrate
Distance from the top surface (mm)
Stress (MPa)
Δσx
(d) Case 4
(e) Case 5
σx (MPa)
600
400
200
0
-200
-400
-600
270
310

FIGURE 8

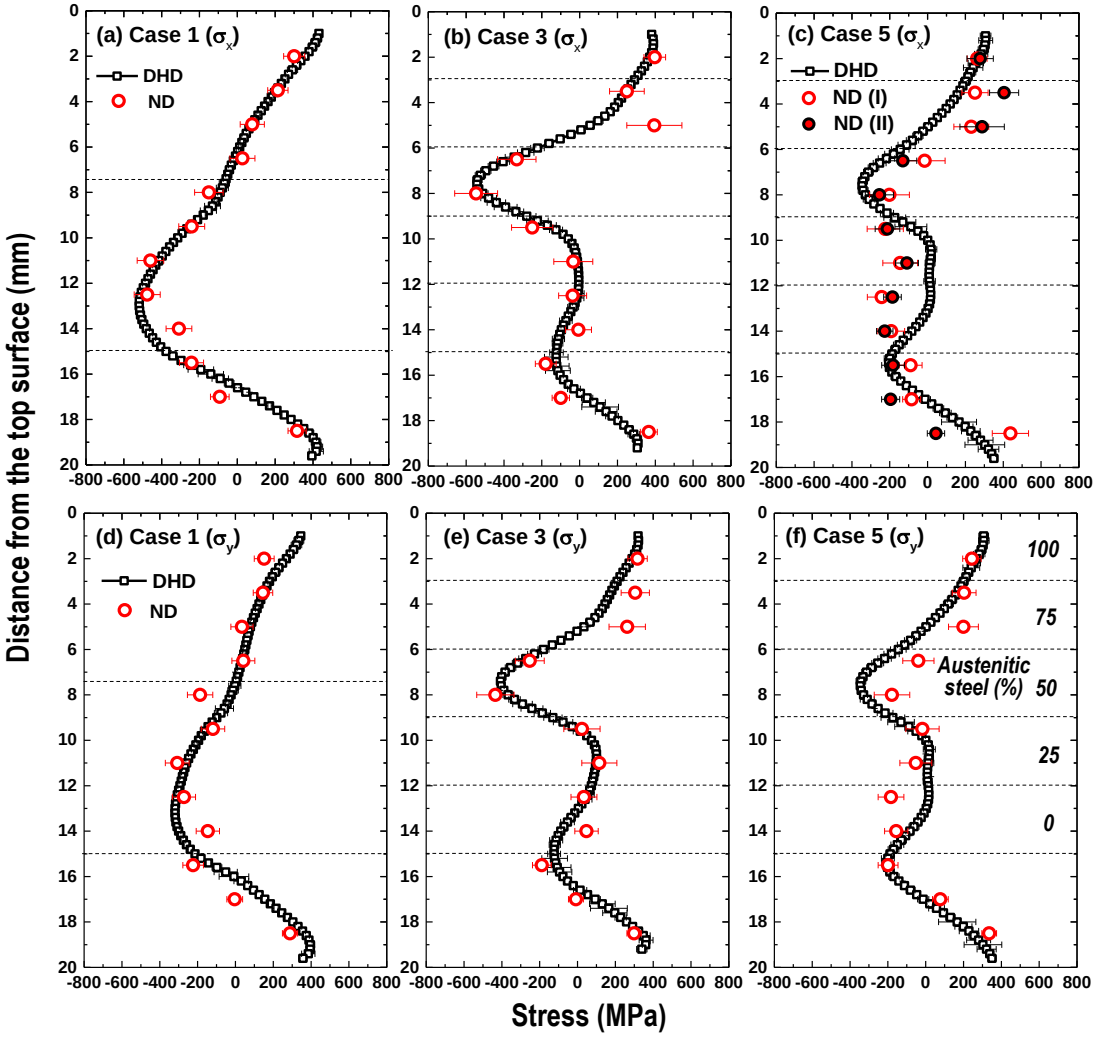
(a) Case 1 (σx)
DHD
ND
(b) Case 3 (σx)
(c) Case 5 (σx)
DHD
ND (I)
ND (II)
(d) Case 1 (σy)
DHD
ND
(e) Case 3 (σy)
(f) Case 5 (σy)
100
75
Austenitic steel (%) 50
25
0
Distance from the top surface (mm)
Stress (MPa)

FIGURE 9

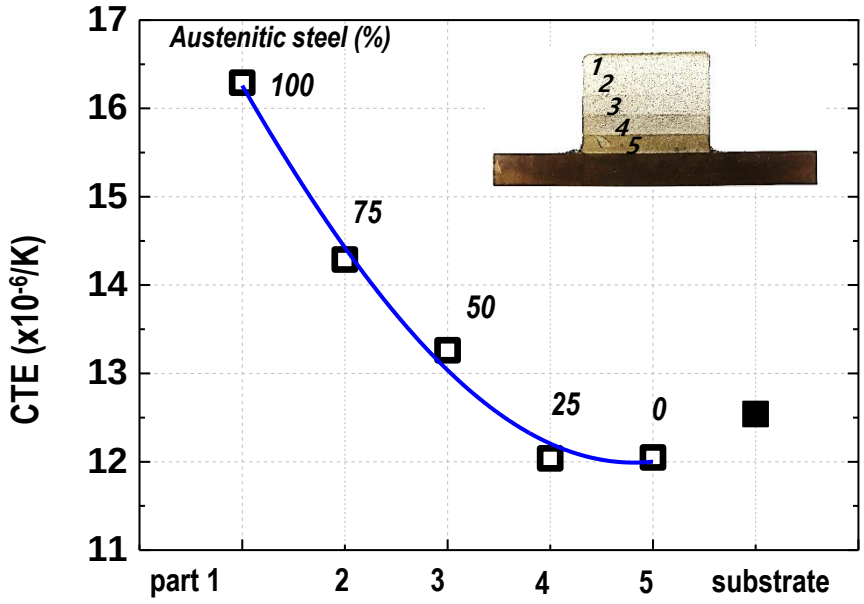
Austenitic steel (%)
100
75
50
25
0
1
2
3
4
5
CTE (x10-6/K)
17
16
15
14
13
12
11
part 1
2
3
4
5
substrate

FIGURE 10

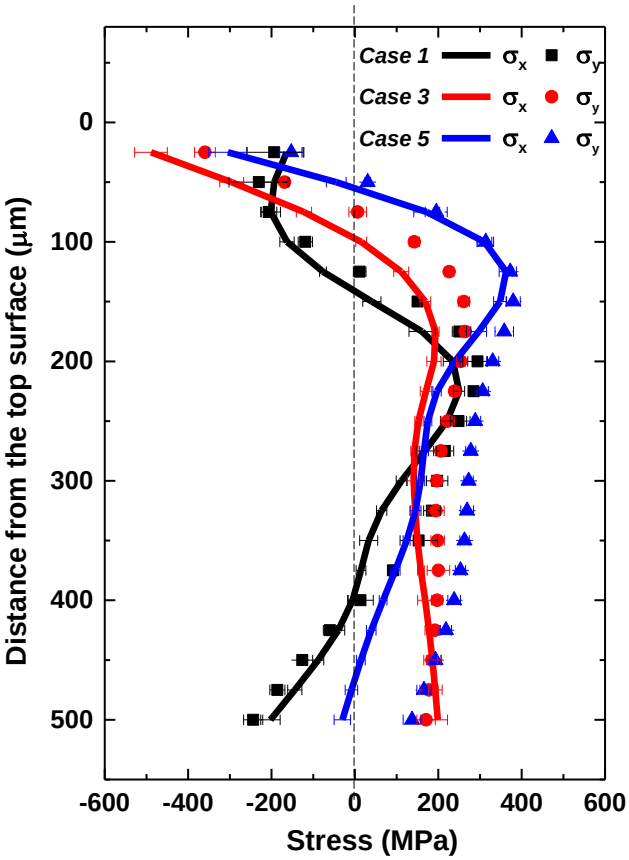
Case 1
σx
σy
Case 3
σx
σy
Case 5
σx
σy
Distance from the top surface (μm)
0
100
200
300
400
500
-600
-400
-200
0
200
400
600
Stress (MPa)

FIGURE 11

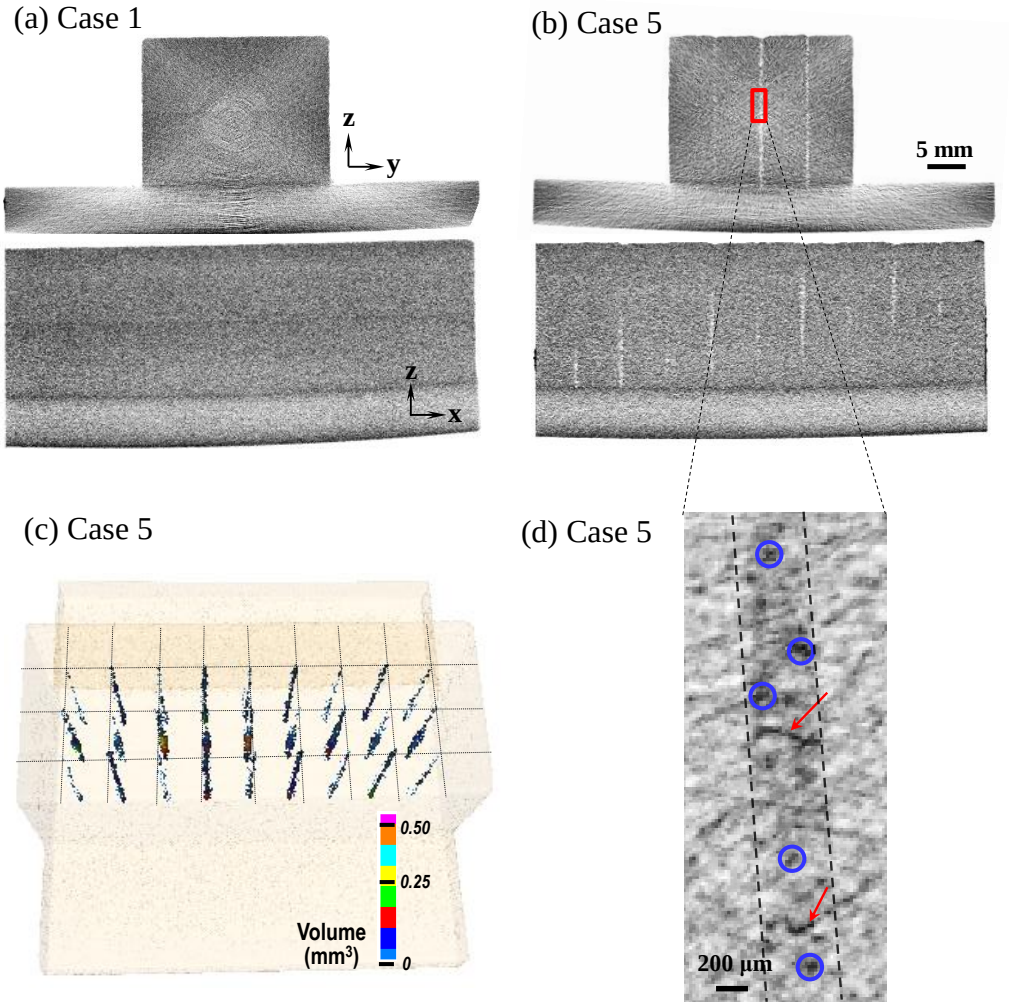
(a) Case 1
z
y
z
x
(b) Case 5
5 mm
(c) Case 5
0.50
0.25
Volume
(mm³)
0
(d) Case 5
200 µm

Table caption

Table. 1. Nominal chemical composition of the austenitic stainless steel powder (316L) and ferritic carbon steel powder (P21), and ferritic steel substrate plate (S45C) for the direct energy deposition (DED) processed functionally graded material (FGM) specimens.

Table 1

Materials	C	Si	Mn	P	S	Cr	Ni	Mo	V	Al	Fe
Austenitic steel (316L,fcc)	0.03	0.75	2.00	0.05	0.03	17.00	12.00	2.50	-	-	65.65
Ferritic steel (P21,bcc)	0.20	0.30	0.30	0.03	0.03	0.40	4.00	0.00	0.20	1.15	93.39
Substrate (steel, S45C, bcc)	0.45	0.25	0.75	0.03	0.035	0.20	0.20	-	-	-	98.08